

# The Nature of Starburst Activity in M 82 <sup>1</sup>

N. M. Förster Schreiber<sup>1</sup>, R. Genzel, D. Lutz

*Max-Planck-Institut für Extraterrestrische Physik, Postfach 1312, D-85741 Garching, Germany*  
 forster@strw.leidenuniv.nl, genzel@mpe.mpg.de, lutz@mpe.mpg.de

and

A. Sternberg

*School of Physics and Astronomy, Tel Aviv University, Ramat Aviv, Tel Aviv 69978, Israel*  
 amiel@wise.tau.ac.il

## ABSTRACT

We present new evolutionary synthesis models of M 82 based mainly on observations consisting of near-infrared integral field spectroscopy and mid-infrared spectroscopy. The models incorporate stellar evolution, spectral synthesis, and photoionization modeling, and are optimized for  $\lambda = 1 - 45 \mu\text{m}$  observations of starburst galaxies. The data allow us to model the starburst regions on scales as small as 25 pc. We investigate the initial mass function (IMF) of the stars and constrain quantitatively the spatial and temporal evolution of starburst activity in M 82. We find a typical decay timescale for individual burst sites of a few million years. The data are consistent with the formation of very massive stars ( $\gtrsim 50 - 100 M_{\odot}$ ) and require a flattening of the starburst IMF below a few solar masses assuming a Salpeter slope  $dN/dm \propto m^{-2.35}$  at higher masses. Our results are well matched by a scenario in which the global starburst activity in M 82 occurred in two successive episodes each lasting a few million years, peaking about  $10^7$  yr and  $5 \times 10^6$  yr ago. The first episode took place throughout the central regions of M 82 and was particularly intense at the nucleus while the second episode occurred predominantly in a circumnuclear ring and along the stellar bar. We interpret this sequence as resulting from the gravitational interaction between M 82 and its neighbour M 81, and subsequent bar-driven evolution. The short burst duration on all spatial scales indicates strong negative feedback effects of starburst activity, both locally and globally. Simple energetics considerations suggest the collective mechanical energy released by massive stars was able to rapidly inhibit star formation after the onset of each episode.

*Subject headings:* galaxies: evolution — galaxies: individual (M 82) — galaxies: starburst — infrared: galaxies — stars: formation

## 1. INTRODUCTION

In recent years, it has become clear that starburst galaxies are important constituents of the

Universe at all accessible redshifts (e.g., Heckman 1998; Adelberger & Steidel 2000; Giavalisco 2002; Shapley et al. 2001, 2003; Chapman et al. 2003). However, despite extensive studies in the past two decades, a detailed and quantitative understanding of the starburst phenomenon is still lacking. Crucial issues that remain open include the evolution and feedback effects of starburst activity, its triggering and quenching mechanisms, and the mass distribution of the stars formed in starbursts.

<sup>1</sup>Current address: Leiden Observatory, PO Box 9513, 2300 RA Leiden, The Netherlands

<sup>1</sup>Based on observations with *ISO*, an ESA project with instruments funded by ESA Member States (especially the PI countries: France, Germany, the Netherlands, and the United Kingdom) and with the participation of ISAS and NASA. The SWS is a joint project of SRON and MPE.

Progress has been hindered by the scarcity of spatially resolved data. Furthermore, high resolution optical and ultraviolet studies are often hampered by severe dust obscuration.

In this context, we have undertaken a study of the archetypal starburst galaxy M 82 based on near-infrared (near-IR) integral field spectroscopy and mid-infrared (mid-IR) spectroscopy. Our observations provide detailed information on key features tracing various components of the interstellar medium and of the stellar population, deep into the obscured star-forming regions. The data, along with results of nebular analysis and population synthesis, are described by Förster Schreiber et al. (2001, hereafter paper I), laying the observational basis essential for the starburst modeling presented in this paper. In a closely related study, Thornley et al. (2000) modeled the mid-IR line emission of 27 starburst galaxies to examine the issues of massive star formation and evolution in starburst environments. Their results are particularly relevant to our modeling of M 82.

By virtue of its proximity and brightness, M 82 is an ideal target for investigations of the starburst phenomenon. Following the seminal paper by Rieke et al. (1980), several authors have applied evolutionary synthesis models to M 82 (Bernlöhr 1992; Rieke et al. 1993; Doane & Mathews 1993; Satyapal et al. 1997; Colbert et al. 1999, among others). However, a number of issues remain controversial. For instance, it is still debated whether the initial mass function (IMF) is biased against low-mass stars (see in particular Rieke et al. 1993 and Satyapal et al. 1997). It has also been suggested that the formation of stars with masses  $\gtrsim 30 M_{\odot}$  may be suppressed (e.g., Puxley et al. 1989). Furthermore, in analyzing the relative distributions of various gaseous and stellar components, some authors have proposed inside-out propagation of starburst activity in M 82 (e.g., McLeod et al. 1993; Satyapal et al. 1997) while others have argued in favour of the opposite scenario (e.g., Shen & Lo 1995; de Grijs et al. 2000; de Grijs, O’Connell, & Gallagher 2001).

The previous models of M 82 were either optimized to best reproduce the global properties or focussed on selected stellar clusters. Given the complexity of M 82, a full understanding requires spatially detailed information of various diagnostics tracing different star formation epochs. Our

new IR data, complemented with results at other wavelengths from the literature, allow us to probe the star formation history in the central regions of M 82 “continuously” in space on scales as small as 25 pc and in time up to at least  $\sim 50$  Myr ago. With the application of starburst models we have developed, we use these data to re-examine the issue of the IMF and constrain the spatial and temporal evolution of the star formation activity. Our model results provide quantitative constraints for the triggering mechanisms and feedback effects of starburst activity in M 82.

The paper is organized as follows. Section 2 summarizes the observational constraints. Section 3 describes the starburst models which are applied to selected regions in § 4. Section 5 presents the spatially detailed modeling. Section 6 discusses the results and § 7 summarizes the paper.

## 2. OBSERVATIONAL CONSTRAINTS

Our modeling of M 82 uses the observations presented and analyzed in paper I. The data consist of near-IR  $H$ - and  $K$ -band integral field spectroscopy at  $R \equiv \lambda/\Delta\lambda \sim 1000$  obtained with the Max-Planck-Institut für extraterrestrische Physik (MPE) 3D instrument (Weitzel et al. 1996) and of  $\lambda = 2.4 - 45 \mu\text{m}$  spectroscopy at  $R \sim 500 - 2000$  from the Short Wavelength Spectrometer (SWS; de Graauw et al. 1996) on board the *Infrared Space Observatory* (ISO; Kessler et al. 1996). The 3D field of view is nearly parallel to the galactic plane, includes the nucleus, and extends to the west out to about 200 pc. The SWS apertures cover regions including and centered on the 3D field of view. The 3D data have a spatial resolution of  $1.5''$ , corresponding to about 25 pc at the distance of M 82 (3.3 Mpc; Freedman & Madore 1988). We complemented these data with results from the literature, providing further essential constraints.

We selected five representative regions for a detailed analysis. These include the “starburst core” of M 82 corresponding to a 500 pc-diameter region centered on the nucleus, the 3D field of view covering the most intense starburst regions, the central 35 pc at the nucleus, and two  $35 \times 35$  pc regions positioned at the brightest Br $\gamma$  sources observed with 3D, which we designated M82:Br1 and M82:Br2 in paper I ( $\approx 10''$  and  $5''$  southwest of the nucleus, respectively). For simplicity, we refer to the latter

three regions as the “nucleus,” “B1,” and “B2.”

For each region, Table 1 lists the main constraints derived in paper I. These include the intrinsic  $K$ -band and Lyman continuum luminosities ( $L_K$  and  $L_{\text{Ly}\alpha}$ )<sup>3</sup>, the total bolometric luminosities from OB and cool evolved stars as well as the separate contribution of OB stars ( $L_{\text{bol}}$  and  $L_{\text{bol}}^{\text{OB}}$ ), the stellar masses ( $M^*$ ), the supernova rates ( $\nu_{\text{SN}}$ ), the CO 1.62 and 2.29  $\mu\text{m}$  bandhead equivalent widths ( $W_{1.62}$  and  $W_{2.29}$ ), and the neon fine-structure line ratio  $[\text{Ne III}] 15.6 \mu\text{m} / [\text{Ne II}] 12.8 \mu\text{m}$ . The values of the  $L_K/L_{\text{Ly}\alpha}$ ,  $L_{\text{bol}}/L_{\text{Ly}\alpha}$ ,  $L_{\text{bol}}^{\text{OB}}/L_{\text{Ly}\alpha}$ ,  $M^*/L_K$ , and  $\nu_{\text{SN}}/L_{\text{bol}}$  are also given. Except for the starburst core, the neon ratio is an “equivalent” ratio as discussed below.

The  $K$ -band continuum luminosities  $L_K$  and the equivalent widths  $W_{2.29}$  are corrected for the contribution and dilution by hot dust emission (which is negligible for  $W_{1.62}$ ). We assumed that 70% of the OB stars’ bolometric luminosity is detected at IR wavelengths ( $\lambda = 5 - 300 \mu\text{m}$ ) as reprocessed emission by dust, and that 30% escapes perpendicular to the galactic disk. The stellar masses  $M^*$  for the nucleus and the starburst core were computed by subtracting the mass of the gas component (mainly in the form of  $\text{H}_2$ ) from the total dynamical mass. Estimates of supernova explosion rates  $\nu_{\text{SN}}$  suffer from rather large uncertainties (see paper I), so related constraints will be used as consistency arguments. Among the nebular emission line ratios sensitive to the ionizing OB stars available from our data sets, we chose  $[\text{Ne III}] 15.6 \mu\text{m} / [\text{Ne II}] 12.8 \mu\text{m}$  for this work. For the starburst core, the ratio is that measured with the SWS, corrected for extinction. For the other regions, we applied the single-star photoionization models of paper I to derive “equivalent” neon ratios, which are those predicted for the OB stars effective temperatures inferred from the observed near-IR H to He recombination line ratios.

We also modeled individual regions corresponding to rebinned  $1'' \times 1''$  pixels covering the 3D field of view in its entirety. The set of constraints for each pixel, from the 3D data and the 12.4  $\mu\text{m}$  map

<sup>3</sup>We use the following definitions:  $L_K$  is the luminosity in the  $K$  bandpass  $\lambda = 1.9 - 2.5 \mu\text{m}$  (Wamsteker 1981) expressed in units of the total solar luminosity  $L_\odot = 3.85 \times 10^{26} \text{ W}$  while  $L_{\text{Ly}\alpha}$  is the Lyman continuum photon emission rate times an average ionizing photon energy of 15 eV.

of Telesco & Gezari (1992), includes the intrinsic  $L_K$ ,  $L_{\text{Ly}\alpha}$ ,  $L_{\text{bol}}^{\text{OB}}$ ,  $W_{2.29}$ , and the equivalent neon ratio. These constraints are the most useful and relevant ones for the spatially-detailed modeling based on the results of the selected regions.

### 3. STARBURST MODELS

Our starburst models combine evolutionary synthesis of stellar clusters with photoionization modeling of the surrounding gas. They are optimized for applications to  $\lambda = 1 - 45 \mu\text{m}$  observations of starburst galaxies. They assume that a given set of constraints applies to a “homogeneous” stellar population, i.e. either a single cluster or an ensemble of clusters with identical IMF shape and cutoffs (see Thornley et al. 2000).

#### 3.1. Prediction of Stellar Properties

We computed the integrated properties of stellar clusters using the evolutionary synthesis code STARS (Sternberg 1998; Thornley et al. 2000). STARS is similar to other codes which have been presented in the literature (e.g., Bruzual & Charlot 1993; Cerviño & Mas-Hesse 1994; Fioc & Rocca-Volmerange 1997; Leitherer et al. 1999). STARS performs conventional synthesis, assigning fixed evolutionary tracks to an appropriate set of mass bins. STARS employs the Geneva stellar tracks (Schaller et al. 1992); for our analysis, we selected the solar-metallicity tracks with normal mass-loss rates. Although the tracks for enhanced mass-loss rates may provide better fits to observations (see Meynet et al. 1994, and references therein), the choice has little impact for this work. The differences in the synthesized properties of interest here are much smaller than those produced, e.g., by varying the IMF parameters and would imply changes  $\leq 1 \text{ Myr}$  in the derived ages, comparable to those from the measurement uncertainties. We adopted a time-independent power-law IMF  $dN/dm \propto m^{-\alpha}$  between lower and upper mass limits  $m_{\text{low}}$  and  $m_{\text{up}}$ . The stars are assumed to form at a rate  $R(t_b) = R_0 e^{-t_b/t_{\text{sc}}}$ , where  $R_0$  is the initial star formation rate (expressed in  $\text{M}_\odot \text{ yr}^{-1}$ ),  $t_b$  is the burst age, and  $t_{\text{sc}}$  is the burst decay timescale.

The integrated spectra of starburst galaxies in the  $1 - 45 \mu\text{m}$  range are dominated at the short-wavelength end by the direct light of cool evolved

stars and at the long-wavelength end by radiation of mostly OB stars that has been reprocessed by interstellar dust and gas. These populations are treated with particular care in STARS. Specifically, the non local thermodynamical equilibrium (non-LTE) model atmospheres of Pauldrach et al. (1998), which supersede the earlier non-LTE atmospheres of Sellmaier et al. (1996), are chosen to represent adequately the spectral energy distribution (SED) of the hottest stars (see also Pauldrach et al. 2001, and references therein). Empirical photometric data are used to better account for the properties of the coolest stars. Finally, the Geneva tracks for intermediate-mass stars have been extended to include the thermally-pulsing asymptotic giant branch phase (TP-AGB), which can contribute significantly to the integrated  $K$ -band luminosity. STARS also predicts the strength of various near-IR stellar absorption features. Further details on the above aspects are given in appendix A.

The Pauldrach et al. (1998) models include the non-LTE radiative transfer and hydrodynamical treatment of radiatively-driven, spherically expanding steady-state winds and account for the combined effects of line blocking and blanketing on the radiative transfer and energy balance. They provide excellent matches to observed high-resolution far-ultraviolet spectra of hot stars (Pauldrach et al. 2001) and nebular photoionization computations which incorporate these model atmospheres successfully reproduce the relative intensities of infrared emission lines measured in Galactic H II regions (Giveon et al. 2002). As discussed by Giveon et al. (2002) and Thornley et al. (2000), the inclusion of the Pauldrach et al. models is critical for the photoionization modeling because their SEDs are significantly harder than for hydrostatic plane-parallel LTE models such as those of Kurucz (1992). Accounting for the TP-AGB phase is most important for the CO bandheads because it results notably in larger equivalent widths (EWs) at ages  $\gtrsim 50$  Myr (see, e.g., Origlia & Oliva 2000). However, as will be seen below, our results do not depend much on this feature.

### 3.2. Prediction of Nebular Properties

We modeled the neon ratio produced in nebulae excited by the integrated stellar SED computed by

STARS using the photoionization code CLOUDY version C90.05 (Ferland 1996). The nebulae were represented as a single gas shell surrounding a central point-like ionizing source. In such “central cluster” models, the nebular conditions are specified by the gas and dust composition, the hydrogen gas density  $n_{\text{H}}$ , and the ionization parameter  $U \equiv Q_{\text{Ly}\alpha} / (4\pi r^2 n_{\text{H}} c)$ , where  $Q_{\text{Ly}\alpha}$  is the intrinsic Lyman continuum photon emission rate of the source,  $r$  is the shell radius, and  $c$  is the speed of light.

We adopted the parameter values derived from the nebular analysis of paper I:  $n_{\text{H}} = 300 \text{ cm}^{-3}$ , an *effective* ionization parameter with  $\log U_{\text{eff}} = -2.3$  dex, and solar photospheric gas-phase abundances (from Grevesse & Anders 1989; Grevesse & Noels 1993, as implemented in CLOUDY v. C90.05). As argued in paper I, a more realistic representation of the H II regions in M 82 consists of a well-mixed distribution of ionizing clusters and gas clouds. The average ionization parameter at the outer boundaries of the gas clouds derived from the observed properties assuming such a “random distribution” model constitutes the appropriate effective value for modeling in the framework of the idealized central cluster geometry. Interestingly, we found nearly identical  $\log U_{\text{eff}}$  throughout the starburst core of M 82 on scales of a few tens of parsecs to  $\sim 500$  pc. As discussed in paper I, this appears to indicate a uniform star formation efficiency across the observed regions.

Following Thornley et al. (2000), we computed the neon ratio for bursts with decay timescale  $t_{\text{sc}} = 1$  Myr by assuming that  $U_{\text{eff}}$  varies proportionally with  $Q_{\text{Ly}\alpha}$  and that the maximum value of  $\log U_{\text{eff}}$  equals  $-2.3$  dex. For bursts with longer decay timescales, we convolved the corresponding star formation rates  $R(t_{\text{b}})$  with the time-dependent neon ratio for the short decay bursts. We neglected the effects of dust grains mixed with the ionized gas within the nebulae; this has little impact on our model results (see § 4.5).

### 3.3. Modeling Procedure

We approached the modeling of M 82 by first making physical and qualitative arguments to constrain the possible ranges for the parameters, and then performed quantitative fits. This led to physically plausible and successful models although they may not be unique. We first investigated,

from the properties of selected regions, the general characteristics of starburst activity: the IMF cutoffs and the typical burst decay timescale (§ 4). Having determined these parameters and identified the most useful age indicators, we then modeled individual regions across the entire 3D field of view to constrain the spatial and temporal evolution of starburst activity (§ 5).

Most of our constraints are sensitive to  $m_{\text{up}}$ ,  $t_{\text{sc}}$ , and  $t_{\text{b}}$ , so we investigated these parameters simultaneously. The total stellar mass depends only on the low-mass IMF (shape and  $m_{\text{low}}$ ), which we examined independently. We used ratios of different properties derived from data obtained at similar wavelengths along with the CO bandheads EWs, minimizing uncertainties from the extinction corrections and from the distance assumed for M82. The exception is  $\nu_{\text{SN}}/L_{\text{bol}}$  but we used it mainly as consistency check because of the uncertainties on  $\nu_{\text{SN}}$  (§ 2). We determined the initial star formation rates  $R_0$  by comparing the predicted luminosities to the measured values. We kept the other parameters constant; the effects of variations in the most critical ones will be discussed when appropriate. Table 2 summarizes the ranges considered or the fixed values adopted for the model parameters.

#### 4. MODELING OF SELECTED REGIONS IN M82

Figure 1 compares the properties of the selected regions from Table 1 to model predictions. The models were computed for  $m_{\text{up}} = 100 M_{\odot}$  and are shown for burst decay timescales of 1 Myr, 5 Myr, 20 Myr, and 1 Gyr. The diagnostics considered are not affected by the low-mass star population so a fiducial  $m_{\text{low}} = 1 M_{\odot}$  was here adopted. This comparison reveals age differences between the regions, in particular between the nucleus (older) and the regions B1 and B2 (younger). The exact ages depend on the upper mass cutoff and burst decay timescale, which we constrained first.

##### 4.1. Upper Mass Cutoff and Burst Timescale

The neon and  $L_{\text{bol}}/L_{\text{Lyc}}$  ratios are our most sensitive diagnostics to the upper mass cutoff. Figure 2 shows model computations for these ratios with  $m_{\text{up}} = 25, 30, 35, 50$ , and  $100 M_{\odot}$ , and for  $t_{\text{sc}} = 1$  and 5 Myr. The upper mass cutoff is best

constrained from the properties of the young massive stars only. Therefore, the observed bolometric luminosities for selected regions in Figure 2 exclude the contribution from cool evolved stars so that the  $L_{\text{bol}}^{\text{OB}}/L_{\text{Lyc}}$  ratios are compared to the models.

Both diagnostics imply similar dominant OB star populations for the various regions considered. The small values of the neon ratio suggest a relative paucity of ionizing photons with energies  $> 3$  Ryd (the ionization potential of  $\text{Ne}^+$ ) while the low  $L_{\text{bol}}^{\text{OB}}/L_{\text{Lyc}}$  ratios imply that lower energy Lyman continuum photons are being produced efficiently. From the comparison with the models, two alternative interpretations are possible: (1) a high  $m_{\text{up}} \gtrsim 50 M_{\odot}$ , a short timescale of at most a few million years, and the softening of the ionizing radiation field attributable to rapid aging of the starburst, or (2) a lower  $m_{\text{up}}$  down to  $\approx 30 M_{\odot}$ , with longer timescales possible. Upper mass cutoffs below  $30 M_{\odot}$  are ruled out, but the data do not allow us to constrain unequivocally  $m_{\text{up}}$  and  $t_{\text{sc}}$  for  $m_{\text{up}} \geq 30 M_{\odot}$ .

As summarized by Thornley et al. (2000), a variety of results on local templates of starburst regions as well as other large-scale starburst systems make high upper mass cutoffs more plausible. In M82, the low  $L_{\text{bol}}^{\text{OB}}/L_{\text{Lyc}}$  values for B1 and B2 can only be reproduced with  $m_{\text{up}} \gtrsim 50 M_{\odot}$ . The neon and  $L_{\text{bol}}^{\text{OB}}/L_{\text{Lyc}}$  ratios measured for all selected regions lie within the ranges determined for the sample of dusty solar-metallicity IR-luminous starburst galaxies of Thornley et al. (2000). These ranges, indicated in Figure 2, are compatible with  $m_{\text{up}} \geq 50 M_{\odot}$  and differences among the sample sources attributable to a range in burst ages.

In addition, the poor correlation in M82 on scales of a few tens of parsecs between the spatial distributions of the near-IR continuum emission and CO bandhead EWs, and that of the ionized gas (e.g.,  $\text{Br}\gamma$  and  $\text{He I } 2.06 \mu\text{m}$ ) and IR dust emission provides strong evidence for short decay timescales in individual burst sites (see the 3D images of paper I; also, e.g., Telesco et al. 1991; Larkin et al. 1994; Satyapal et al. 1997). Since red supergiants dominate the near-IR continuum emission in M82 (§ 4.3), the poor correlation implies that star formation activity was not maintained locally at high levels longer than the typical main-sequence lifetime of the most massive

red supergiants progenitors ( $\approx 5$  Myr). This situation is reminiscent of the nucleus of M83, where Puxley et al. (1997) found that the K-band continuum emission and CO bandhead strength are spatially anticorrelated with the Br $\gamma$  EW, which they interpreted, together with starburst models, as indicating an evolutionary sequence and burst timescales of 1 – 5 Myr. Massive star formation is expected to inhibit further star formation locally already after a few million years owing to strong stellar winds and supernova explosions disrupting the surrounding interstellar medium (ISM). The  $\sim 100$  pc-size gas hole around the brightest radio supernova remnant 41.9 + 58 seems to provide a particularly striking example of such effects in M82 (e.g., Weiß et al. 1999).

The most remarkable outcome of our models is that for  $m_{\text{up}} \geq 50 M_{\odot}$ , the OB star-dominated properties of the 3D field of view and the starburst core imply short burst decay timescales on large spatial scales ( $\sim 100 - 500$  pc). This is not due to a few regions dominating the integrated properties; for instance, B1 and B2 contribute together less than 15% to the  $L_{\text{Lyc}}$  and  $L_{\text{bol}}^{\text{OB}}$  measured in the 3D field of view. Our results suggest that in M82 starburst activity can have strong negative feedback effects globally as well. We discuss this point further in § 6.

#### 4.2. Successive Starburst Events

In the rest of this paper, we will adopt  $m_{\text{up}} = 100 M_{\odot}$  and a representative  $t_{\text{sc}} = 1$  Myr as justified above. Examination of Figures 1 and 2 then reveals that for each region, there is a systematic increase in burst age from that implied by the tracers of OB stars (neon and  $L_{\text{bol}}^{\text{OB}}/L_{\text{Lyc}}$  ratios) to that inferred from the tracers of cool evolved stars (CO bandheads). The differences are about 5 Myr. The  $L_K/L_{\text{Lyc}}$  ratios, measuring the relative populations of these stellar components, correspond to intermediate ages.

Figure 3 illustrates the difficulty of single burst models to meet simultaneously the constraints for each of the selected regions. The figure compares the regions’ properties to evolutionary tracks for single bursts in diagrams of the neon,  $L_{\text{bol}}/L_{\text{Lyc}}$ , and  $L_K/L_{\text{Lyc}}$  ratios versus  $W_{2.29}$ . At ages corresponding to the measured values of  $W_{2.29}$ , models for  $t_{\text{sc}} = 1$  Myr and  $m_{\text{up}} = 100 M_{\odot}$  predict neon ratios 10 (B1) to 34 (nucleus) times lower than

measured,  $L_{\text{bol}}/L_{\text{Lyc}}$  ratios 6 (nucleus) to 23 (B2) times higher, and  $L_K/L_{\text{Lyc}}$  ratios 4 (nucleus) to 33 (B2) times higher. The constraints are still not satisfied simultaneously when augmenting the burst decay timescale to 5 Myr with, in particular, predicted neon ratios about an order of magnitude higher than measured at ages corresponding to the observed values of  $W_{2.29}$ . Allowing for lower  $m_{\text{up}}$  down to  $50 M_{\odot}$  only worsens the discrepancies.

The age sequence between the various diagnostics may suggest that the hot massive stars and the cool evolved stars belong to populations formed in distinct, successive starburst events. In this scenario, the “young bursts” account for most of the ionizing radiation while the “old bursts” dominate the near-IR properties. Rieke et al. (1993) first proposed such two-burst models of the entire starburst core of M82 for similar reasons. We thus considered models consisting of two sequential bursts, each with  $t_{\text{sc}} = 1$  Myr and  $m_{\text{up}} = 100 M_{\odot}$ , and separated in time by more than one decay timescale. Figure 4 shows similar evolutionary tracks as Figure 3 for the best-fit time separation and relative burst intensities for each region derived in § 4.3. From Figures 3 and 4, it is also difficult to disentangle between single and two-burst models. However, since the neon and  $L_{\text{bol}}^{\text{OB}}/L_{\text{Lyc}}$  ratios seem to favour the shortest decay timescales, successive short bursts could provide a natural explanation for the observed strength of the CO bandheads. The two-burst scenario also appears plausible in view of the morphology and nearly edge-on orientation of M82 (§ 6).

We remark that given the uncertainties of the data and models, it may be possible to find single bursts with finely-tuned parameters which reproduce all the observed properties. Exponentially decaying bursts with  $t_{\text{sc}}$  intermediate between 1 and 5 Myr, for instance, could meet the neon ratio constraint while violating the  $L_{\text{bol}}/L_{\text{Lyc}}$  and  $L_K/L_{\text{Lyc}}$  constraints at a level that is more severe than for the double bursts but probably still acceptable. As another example, allowing lower  $m_{\text{up}}$  down to  $30 M_{\odot}$  together with longer  $t_{\text{sc}}$  of 10 – 20 Myr for single bursts may improve the fit to the neon ratios but the mismatch is only redistributed to the other properties. Similar difficulties in modeling comparable sets of constraints have been encountered for other dusty IR-selected starbursts, e.g., by Engelbracht et al. (1998) for

NGC 253 and Goldader et al. (1997) for a sample of (ultra)luminous IR galaxies. With our data and models of M 82, together with the obvious complexity of the problem, it is not possible to find a unique solution.

### 4.3. Burst Age and Strength

Adopting the two-burst scenario as working hypothesis, we constrained the age of the young bursts from the neon and  $L_{\text{bol}}^{\text{OB}}/L_{\text{Lyc}}$  ratios, and of the old bursts from the CO bandheads. The initial star formation rates  $R_0$  (with  $m_{\text{low}}$  fixed at  $1 M_{\odot}$ ) were adjusted so that the total contribution from both bursts to  $L_{\text{Lyc}}$  and  $L_K$  reproduces the observed values. For identical IMF parameters and burst decay timescales, the values of  $R_0$  provide a meaningful measure of the relative strengths of the bursts.

For the young bursts, the ages inferred from each indicator agree marginally, the neon ratio implying slightly older ages. This discrepancy would not be solved by other choices of  $m_{\text{up}}$  and  $t_{\text{sc}}$ . The difference is comparable to the burst timescale and, in view of the measurements and modeling uncertainties, is probably not significant. The  $L_{\text{bol}}^{\text{OB}}/L_{\text{Lyc}}$  ratio may trace a slightly different population as it is sensitive to a somewhat lower stellar mass range than the neon ratio is. The effects of a distribution of cluster masses and luminosities or of dust grains within the nebulae, neglected here, would increase the discrepancy (§ 4.5). We therefore assigned equal weights to the diagnostic ratios.

For the old bursts, an accurate age determination is only possible for the nucleus. It has very deep CO bandheads which the models reproduce only at ages of 8 – 15 Myr, consistent with the average spectral type K5 I derived from detailed spectral synthesis in paper I. The EWs at the nucleus further support short burst timescales: for  $t_{\text{sc}} \geq 5$  Myr, the contribution from older populations with shallower bandheads and/or photospheric and nebular featureless continuum emission from OB stars results in predicted EWs lower than observed, for any burst age. Figure 5 indicates that older ages when intermediate-mass stars reach the end of the asymptotic giant branch ( $\sim 50$  Myr – 1 Gyr) are also ruled out from  $W_{2.29}$ .

For the other selected regions, we can set firm

lower limits on the ages but the EWs alone do not provide strong constraints on upper limits. For comparison with our data and models, we indicate in Figure 5 the ranges observed by Oliva et al. (1995) for old (1–10 Gyr) stellar populations characteristic of the central regions of elliptical galaxies and bulges of spiral galaxies (hereafter “normal populations”). The EWs at B1 are somewhat lower than for normal populations and may indicate an early stage when the first red supergiants appear. For B2, the 3D field of view, and the starburst core, they are slightly higher and imply possible upper limits on the age of  $\approx 50$  Myr and on the timescale of  $\approx 5$  Myr.

The  $M^*/L_K$  ratio provides an additional constraint. Empirical determinations for normal populations lie in the range  $10\text{--}30 M_{\odot}/L_{\odot}$  (Devereux, Becklin, & Scoville 1987; Oliva et al. 1995; Hunt et al. 1999).<sup>4</sup> As argued in paper I, the substantially lower values  $\sim 1 M_{\odot}/L_{\odot}$  measured for M 82 between radii of  $\approx 10$  and 250 pc indicate very large contributions from red supergiants to the near-IR continuum emission, even in regions of low surface brightness. Consequently, ages  $\lesssim 50$  Myr are the most plausible. We adopted the solutions corresponding to the rising part of the predicted EWs with  $t_{\text{sc}} = 1$  Myr but older ages of 15 – 30 Myr are also possible. Our choice implies lower  $R_0$  for the old bursts since the predicted  $L_K$  peaks around 10 Myr. The younger age solutions are unaffected by uncertainties related to numerical fluctuations due to our conventional synthesis technique and to our TP-AGB implementation, which may become a concern at ages  $\gtrsim 50$  Myr (see appendix A).

### 4.4. Model Results for Selected Regions

Tables 3 and 4 report our two-burst model results for the selected regions. The derived burst strengths outline the particular intensity of starburst activity in the central few tens of parsecs of M 82 about 10 Myr ago. Our model for the starburst core agrees well with the results of Rieke et al. (1993) who found that separate bursts occurring about 5 and 13 Myr ago, each lasting a few million years, could reproduce the observed prop-

<sup>4</sup>Our units for the  $M^*/L_K$  ratio differ from the conventional definition expressed in  $(M/L_K)_{\odot}$ . The quoted range has been computed in  $M_{\odot}/L_{\odot}$  from the data presented in the given references, assuming a  $K$  bandpass  $\lambda = 1.9\text{--}2.5 \mu\text{m}$  and expressing  $L_K$  in  $L_{\odot} = 3.85 \times 10^{26}$  W.

erties. The small differences between our model and theirs reflect mainly differences in the adopted set of constraints and model assumptions (such as their choice of Gaussians to represent the star formation rate).

We estimated the formal uncertainties on the relative burst ages and strengths  $R_0$  by varying in turn the observational constraints within the ranges corresponding to the measurement errors. They are typically  $\lesssim 0.5$  Myr and 25% – 40% for the ages and strengths, respectively. For the old bursts, the minimum age is fairly well constrained by the CO bandhead EWs whereas the maximum age from the quoted uncertainties constitutes a lower limit since we did not account here for the older possible solutions. The absolute burst ages and intensities may suffer from larger uncertainties related, e.g., to the burst decay timescale and shape of the star formation rate. The relative ages and intensities are less affected because the evolution of the properties considered are dominated by stellar evolution during the early phases of a burst and for decay timescales comparable to the main-sequence lifetime of the most massive stars.

Figure 6 illustrates the results for the most relevant properties:  $L_K$ ,  $L_{\text{Lyc}}$ ,  $L_{\text{bol}}$ ,  $W_{2.29}$ ,  $W_{1.62}$ , and the neon ratio. For each region, the curves show the variations of the properties as a function of the time elapsed since the onset of the old burst and are normalized to the observed values. They represent the combination of the two bursts, weighted by the respective values of  $R_0$  for each burst. The models for all regions reproduce the main constraints within a factor of three or better. The masses computed for the nucleus and the starburst core are, however, substantially lower than the measured values. The mass is very sensitive to the lower cutoff and shape of the IMF, which we discuss in § 4.6.

Our results are roughly consistent with the constraints imposed by  $\nu_{\text{SN}}$  and  $10^{12} \nu_{\text{SN}}/L_{\text{bol}}$ . A good agreement for the regions observed with 3D is not expected because of the large uncertainties in deriving  $\nu_{\text{SN}}$  from [Fe II] 1.644  $\mu\text{m}$  line fluxes, as discussed in paper I. The ages inferred for the old bursts satisfy the “timing constraint” implied by the extent of the X-ray halo tracing the supernova-driven wind of M 82, which requires a minimum starburst age of about 10 Myr (Heckman, Armus, & Miley 1990; Rieke et al. 1993; Lehnert, Heck-

man, & Weaver 1999).

#### 4.5. Model Uncertainties

We investigated the effects of various sources of uncertainties on our model results so far, including the assumption of a homogeneous cluster population, the nebular parameters, the shape of the IMF, and the synthetic model atmospheres. Their effects have been described for the neon ratio by Thornley et al. (2000) whom we refer to for further details. Figure 7 shows in addition the effects on the  $L_{\text{bol}}/L_{\text{Lyc}}$  and  $L_K/L_{\text{Lyc}}$  ratios, and on  $W_{2.29}$ . None of the above sources of uncertainties affect our conclusions concerning the upper mass cutoff of the IMF or the ages and relative intensities derived for the bursts. While possible alternative assumptions or variations of the nebular parameters and IMF shape result in measurable differences in the model predictions, the effects remain small compared to those of aging or changes in  $m_{\text{up}}$ .

In particular, the largest effects are obtained for a “heterogeneous” population of stellar clusters following the luminosity function (LF) derived by Thornley et al. (2000)<sup>5</sup>. This LF was constructed assuming it reflects a cluster mass function and imposes a distribution in effective  $m_{\text{up}}$  of clusters (at fixed IMF slope and  $m_{\text{low}}$ ). The large proportion of small clusters results in a “down-weighting” effect with, for instance, lower neon ratios and shallower CO bandheads due to the reduction in relative population of massive stars. However, the effects are but a factor of two or less. Similar differences for the neon ratio are obtained by varying the ionization parameter within the possible range  $-2.5 \leq \log U_{\text{eff}} \leq -2$  for M 82 (paper 1) or adopting the softer Kurucz (1992) SEDs for hot stars instead of the Pauldrach et al. (1998) SEDs (see Thornley et al. 2000). The effects of dust within the H II regions, illustrated with the Orion nebular composition, are significantly smaller. By absorbing ionizing photons, dust would also reduce the  $L_{\text{Lyc}}$  in the models. This is difficult to quantify, but the resulting increase in synthesized  $L_{\text{bol}}/L_{\text{Lyc}}$  and  $L_K/L_{\text{Lyc}}$  would only imply younger ages and keep the inferred burst decay timescales short.

<sup>5</sup>For reference, the LF in terms of cluster H ionizing rate  $Q_{\text{Lyc}}^{\text{cl}}$  is  $dN/d(\log Q_{\text{Lyc}}^{\text{cl}}) \propto (Q_{\text{Lyc}}^{\text{cl}})^{-\beta}$ , with  $\beta = 0.19$  for  $Q_{\text{Lyc}}^{\text{cl}} = 10^{45} - 10^{49.5} \text{ s}^{-1}$  and  $\beta = 1$  for  $Q_{\text{Lyc}}^{\text{cl}} = 10^{49.5} - 10^{53} \text{ s}^{-1}$ .



Figure 8 shows that the alternative IMFs we considered, from Miller & Scalo (1979) and that derived by Eisenhauer et al. (1998) for the Galactic high-mass star-forming region NGC 3603, bracket the range of slopes at intermediate and high masses determined for young clusters and OB associations in the Milky Way and Large Magellanic Cloud (e.g., Hunter et al. 1997 and references therein; Brandl et al. 1996; Massey & Hunter 1998; Kroupa 2001). Changes in the IMF shape have the smallest effects in our models. As a consequence, our set of observational constraints does not allow us to investigate the shape of the intermediate- and high-mass IMF in M 82.

Potential problems with the stellar evolutionary tracks represent an additional source of uncertainties. A detailed discussion is beyond the scope of this paper but we briefly mention two points relevant to this work. Origlia and co-workers (Origlia et al. 1999; Origlia & Oliva 2000) warned that model predictions of the CO bandheads can be significantly underestimated at ages  $\gtrsim 10$  Myr if the TP-AGB phase is not accounted for (see also Charlot & Bruzual 1991; Lançon & Rocca-Volmerange 1994) and because of the possible inadequacy of current stellar tracks for the evolution of massive stars in the red supergiant phase, most severely at sub-solar metallicities. Our starburst models account for the TP-AGB (see appendix A) and use solar-metallicity tracks as appropriate for M 82 (paper I), reducing the impact of these uncertainties on our results. Furthermore, the maximum age from the CO bandheads would be most affected, and much less the minimum age so that the above uncertainties have little consequences on the age sequence suggested by our observational constraints. This result would be more affected if the stellar tracks significantly underpredict the number of very luminous but relatively cool stars ( $\log L_{\text{bol}} > 5.75$ ,  $\log T_{\text{eff}} < 4.5$ ), a possibility raised by Thornley et al. (2000) in their discussion of the Galactic Center. With correspondingly lower predicted neon ratios, the constraints might be more clearly accommodated with single bursts of somewhat longer durations. However, this point remains to be thoroughly investigated.

#### 4.6. Low-mass End of the IMF

The low-mass IMF for the starburst population in M 82 has long been debated. Various au-

thors argued that it is deficient in stars with initial masses below  $\approx 3 M_{\odot}$  compared to the solar neighbourhood IMF (Rieke et al. 1980, 1993; Bernlöhr 1992; Doane & Mathews 1993). The studies by Rieke and coworkers have been the most influential. Rieke et al. (1980) argued for a sharp truncation of the IMF at  $3.5 M_{\odot}$ , with no stars formed below this cutoff. Rieke et al. (1993) modified this conclusion and argued that while the IMF may extend down to  $0.1 M_{\odot}$ , the slope flattens significantly near  $3 M_{\odot}$ , at a substantially higher mass than in the solar neighbourhood (near  $0.5 M_{\odot}$ ; see, e.g., Kroupa 2001 and references therein). More recently, Satyapal et al. (1997) challenged these hypotheses and modeled the integrated  $K$ -band luminosity of M 82 with a Salpeter IMF down to  $0.1 M_{\odot}$  without using up more than  $\approx 35\%$  of the total dynamical mass in the starburst, a reasonable upper limit.

The origin of the controversy resides primarily in the notable differences in observational constraints and model assumptions between the various studies. Here, we reexamine the issue of the low-mass IMF in M 82 in light of our new data and models. We consider two regions for this purpose: the nucleus (central 35 pc) and the starburst core (central 500 pc).

##### 4.6.1. Reexamination of the Low-mass IMF

Among our constraints, the stellar mass  $M^*$  is the only one sensitive to the low-mass star population. We computed this critical quantity by subtracting the mass of the gaseous component  $M_{\text{gas}}$  from the total dynamical mass  $M_{\text{dyn}}$  (see paper I for details). We derived the enclosed  $M_{\text{dyn}}$  as a function of projected radius from position-velocity maps of the millimeter CO  $J = 1 \rightarrow 0$ , [Ne II]  $12.8 \mu\text{m}$  and [S III]  $9069 \text{\AA}$  line emission (Shen & Lo 1995; Achtermann & Lacy 1995; McKeith et al. 1993) combined with the result of stellar velocity dispersion measurements at the nucleus based on the CO  $2.29 \mu\text{m}$  bandhead by Gaffney, Lester, & Telesco (1993). We estimated  $M_{\text{gas}}$ , accounting for molecular and ionized gas, from the CO  $J = 1 \rightarrow 0$  map of Shen & Lo (1995) using the CO intensity to  $\text{H}_2$  column density conversion factor derived by Wild et al. (1992) from multi-line radiative transfer analysis and from the Lyman continuum luminosities. The  $M^*$  for the nucleus and the starburst core are  $7.9 \times 10^7$  and  $6.1 \times 10^8 M_{\odot}$ , respectively.

We investigated the low-mass IMF (shape and cutoff) by comparing the mass of stars predicted by the model bursts  $M_{\text{stb}}^*$  with the  $M^*$  derived for each region. In this comparison, allowance has to be made for a possible stellar population pre-dating the starburst, which can contribute to the measured stellar mass, so that the computed  $M_{\text{stb}}^*$  does not exceed a plausible fraction of  $M^*$ . To estimate this fraction, we followed the argument of McLeod et al. (1993). Tidal interaction with M81 presumably induced the starburst in M82; numerical simulations indicate that the perturbations resulting from such encounters can efficiently drive large amounts of gas towards the nuclear regions and that before the gas mass equals the mass in preexisting stars, self-gravitation in the gas should trigger a starburst with short timescale compared to the gas settling time (e.g., Hernquist 1989; Mihos & Hernquist 1994, 1996). Thus,  $M_{\text{stb}}^*$  unlikely exceeds half of  $M_{\text{dyn}}$  in M82. In our analysis, we adopted a conservative upper limit for  $M_{\text{stb}}^*$  of 50% of the total *stellar* mass  $M^*$ . We did not account for the gas mass returned to the ISM via stellar winds and supernova explosions, or expelled out of the galaxy in the starburst wind. Since massive stars contribute most to the mass return for the burst ages  $\lesssim 20$  Myr relevant here but do not dominate  $M_{\text{stb}}^*$ , these effects can be neglected to first order but will be further addressed below.

Our two-burst models for the nucleus and the starburst core (Tables 3 and 4) use only 9% and 33%, respectively, of the stellar masses for a Salpeter IMF slope between  $m_{\text{low}} = 1 M_{\odot}$  and  $m_{\text{up}} = 100 M_{\odot}$ , but this choice of  $m_{\text{low}}$  was arbitrary. Figure 9 shows the burst masses required to reproduce the observed luminosities ( $L_K$  and  $L_{\text{Lyc}}$ ) computed for  $m_{\text{low}}$  in the range  $0.1 - 5 M_{\odot}$ , with a Salpeter slope and for the same burst ages and decay timescales. For the nucleus, the bursts never use up more than 30% of the measured  $M^*$ . On the other hand, the burst mass for the starburst core reaches 50% of  $M^*$  at  $m_{\text{low}} = 0.4 M_{\odot}$  and equals  $M^*$  at  $m_{\text{low}} \approx 0.1 M_{\odot}$ . For the mass involved in the starburst not to exceed our adopted limit would require a sharp cutoff at  $0.4 M_{\odot}$  for a Salpeter IMF. Alternatively, allowing the IMF to extend down to  $0.1 M_{\odot}$ , a flattening of the IMF at low masses would be required to reduce the increase in  $M_{\text{stb}}^*$  with decreasing  $m_{\text{low}}$  so that  $M_{\text{stb}}^* \leq 50\%$  of  $M^*$ . With only one constraint

available, our analysis does not allow us to break the degeneracy between the cutoff and the shape of the low-mass IMF.

#### 4.6.2. Factors Influencing the Low-mass IMF Determination

The  $M_{\text{stb}}^*$  predicted by the models is determined by the absolute luminosities. This makes inferences on the low-mass IMF very sensitive to the extinction corrections applied, to the star formation history, and to the shape of the IMF at higher masses. The first point has been extensively discussed by McLeod et al. (1993), Rieke et al. (1993), and Satyapal et al. (1997). In that respect, our intrinsic luminosities correspond to the higher ranges reported in the literature and therefore impose more stringent constraints. In particular, the  $L_K$  used by Satyapal et al. (1997) and the lower limit considered by Rieke et al. (1993) are both smaller than our value ( $5 \times 10^8$  and  $7.8 \times 10^8 L_{\odot}$  compared to  $1.3 \times 10^9 L_{\odot}$  for a  $\lambda = 1.9 - 2.5 \mu\text{m}$   $K$  bandpass and the photometric system of Wamsteker 1981 we adopted). With our two-burst models, they allow  $m_{\text{low}}$  down to  $0.2 M_{\odot}$  or less, as shown in the bottom panel of Figure 9 (the mass constraints are similar between all three studies).

The star formation history can also significantly alter the conclusions about the low-mass IMF since longer or older bursts tend to use up more mass. In this regard, however, our conclusions above for a Salpeter IMF differ from those of Satyapal et al. (1997) mainly because of the different  $L_K$  adopted. In terms of  $M_{\text{stb}}^*$ , their single burst model for the starburst core, with an age of 10 Myr and a short duration, is comparable to our two-burst model in which the old burst with an age of 9 Myr contributes 75% of the total burst mass for this region. Comparison with the models of Rieke et al. (1993) is less straightforward; our two-burst model is very similar to theirs with respect to burst ages and durations but the adopted IMFs are very different.

For the young ages of interest here, the various luminosities are dominated by high-mass stars, so that the relative slope of the IMF between different mass ranges is particularly critical in constraining the low-mass IMF. For instance, IMFs which steepen at high masses are less efficient at converting the mass into luminosity. In order

to reproduce the luminosities, they require larger  $M_{\text{stb}}^*$ . To illustrate this, we considered three alternative IMFs: the Miller & Scalo (1979) IMF for the solar neighbourhood, the IMF proposed by Rieke et al. (1993) for M82 (their “IMF 8”), and the IMF of Eisenhauer et al. (1998) for NGC 3603. Eisenhauer et al. derived the NGC 3603 IMF based on near-IR adaptive optics observations down to  $1 M_{\odot}$ , their detection limit. For our purposes, we allowed extensions below  $1 M_{\odot}$  using the slope determined in the  $1 - 15 M_{\odot}$  range. Table 5 gives the parameters of the IMFs (see also Figure 8) and Figure 9 shows the variations of the burst masses versus  $m_{\text{low}}$  computed with each of them.

For the range  $0.1 - 100 M_{\odot}$ , the mass fraction locked in stars less massive than  $1 M_{\odot}$  is significantly smaller for the Miller & Scalo IMF compared to the Salpeter IMF (44% and 61%), while the corresponding fractions for stars more massive than  $10 M_{\odot}$  are nearly identical (8% and 12%, respectively). However, properties such as  $L_K$ ,  $L_{\text{bol}}$ , and  $L_{\text{Lyc}}$  are steeply increasing functions of the stellar mass and the Miller & Scalo IMF is much steeper at the high-mass end than the Salpeter IMF. Consequently, normalizing to the same luminosities, the Miller & Scalo IMF predicts substantially more mass than the Salpeter IMF, with  $M_{\text{stb}}^*$  larger by up to a factor of two in our models. The Rieke et al. (1993) IMF is very similar to the Miller & Scalo IMF but with the first inflection point moved up from  $1 M_{\odot}$ , giving particular emphasis on the intermediate-mass range. Of the various IMFs they explored, such modifications to solar-neighbourhood type IMFs were the most successful at reproducing their set of constraints. Finally, compared to the Rieke et al. (1993) IMF, that of Eisenhauer et al. (1998) emphasizes less the intermediate-mass range but has a larger proportion of stars above  $10 M_{\odot}$  (40% versus 23% of the total mass between 1 and  $100 M_{\odot}$ ), implying much higher mass-to-luminosity conversion efficiency.

Figure 9 shows that for the central 35 pc of M82, the low-mass IMF remains unconstrained for any of the three alternative IMFs: the computed  $M_{\text{stb}}^*$  never exceeds 35% of the measured  $M^*$  with  $m_{\text{low}}$  down to  $0.1 M_{\odot}$ . The case of the starburst core is again more restrictive. With the Miller & Scalo (1979) IMF, more than 50% of the stellar mass is involved in the bursts for  $m_{\text{low}} \leq 2 M_{\odot}$ . If

we allow for stars down to  $0.1 M_{\odot}$  to form, we conclude as Rieke et al. (1993) that a displacement of the first inflection point to higher masses is then needed to effectively reduce  $M_{\text{stb}}^*$ . With our data and models, though,  $M_{\text{stb}}^*$  still exceeds half of  $M^*$  at  $m_{\text{low}} \leq 1 M_{\odot}$  if we adopt the Rieke et al. IMF. The Eisenhauer et al. (1998) IMF allows us to extend the IMF with the same  $\alpha = 1.73$  power-law index from  $15 M_{\odot}$  down to  $0.1 M_{\odot}$  without using up more than 30% of the stellar mass in the bursts. Interestingly, if we assume both the IMF and the  $K$ -band luminosity of Rieke et al. (1993), the  $M_{\text{stb}}^*$  remains well below 50% of  $M^*$  over the entire range of  $m_{\text{low}}$  (dashed line in the bottom panel of Figure 9).

Another consideration worth pointing out is the mass loss via massive stars winds and supernova explosions, which is important already within a few million years of the onset of star formation (see, e.g., Leitherer et al. 1999). In particular, the mass returned to the ISM could have been entrained out of M82 in the starburst wind, in which case our  $M^*$  constraint would be missing some fraction or, alternatively, the predicted  $M_{\text{stb}}^*$  curves of Figure 9 would decrease accordingly. An estimate of the effect is difficult because of the unknown amount of returned mass actually driven away in the starburst wind. As an illustration, we may consider the extreme case in which massive stars  $\gtrsim 10 M_{\odot}$  lose all their mass within  $\approx 20$  Myr, and that all ejectae are carried out of M82 by the starburst wind. For a Salpeter IMF extending from 1 to  $100 M_{\odot}$ , the range  $\geq 10 M_{\odot}$  accounts for 31% of the total mass so that at most  $\approx 30\%$  of  $M_{\text{stb}}^*$  would be lost and expelled. This fraction varies with  $m_{\text{low}}$ , up to  $\approx 50\%$  at  $3 M_{\odot}$  and down to  $\approx 10\%$  at  $0.1 M_{\odot}$ , and more generally depends on all IMF parameters. The overall impact is to relax the requirements on the low-mass IMF but the effect is not likely to be more important than the other factors discussed above.

#### 4.6.3. Additional Remarks

In view of the uncertainties involved and the lack of strong constraints on the shape of the IMF, the low-mass IMF in M82 remains elusive and only general statements can be made. If stars formed down to  $0.1 M_{\odot}$ , our data and models may indicate a substantial flattening of the starburst IMF below a few  $M_{\odot}$ , assuming a Salpeter

slope at higher masses. This requirement would be alleviated for a flatter intermediate- and high-mass IMF or for less conservative limits on  $M_{\text{stb}}^*$ . A bias against the formation of low-mass stars has been suggested for other starburst galaxies as well (e.g., Augarde & Lequeux 1985; Wright et al. 1988; Olofsson 1989; Nakagawa et al. 1989; Prestwich, Joseph, & Wright 1994). Engelbracht et al. (1996, 1998) concluded for NGC 6946 and NGC 253 that the IMF proposed by Rieke et al. (1993) for M 82 is more compatible with the observations than a solar-neighbourhood IMF, while Alonso-Herrero et al. (2001) found that the IMF in NGC 1614 may be even more biased towards high-mass stars.

Kinematic mass-to-light ratios have been obtained for a few individual luminous stellar clusters in M 82, from velocity dispersion measurements combined with high resolution *Hubble Space Telescope* (*HST*) imaging. Using optical data obtained for the super star cluster “M 82-F”  $\approx 450$  pc southwest of the nucleus and an age estimate of 60 Myr, Smith & Gallagher (2001) concluded that the cluster IMF is top-heavy and requires a low-mass cutoff at  $2 - 3 M_{\odot}$  for an  $\alpha = 2.3$  slope. McCrady, Gilbert, & Graham (2003) studied two younger ( $\sim 10^7$  yr) clusters roughly 180 pc southwest of the nucleus based on near-IR observations. For an IMF with  $\alpha = 1.3$  at  $0.1 - 0.5 M_{\odot}$  and  $\alpha = 2.3$  at  $0.5 - 100 M_{\odot}$  (based on Kroupa 2001), their data support a relative deficiency at  $\lesssim 1 M_{\odot}$  for one cluster but allow  $m_{\text{low}}$  down to  $0.1 M_{\odot}$  for the other. In their revision of the Smith & Gallagher (2001) analysis of M 82-F, using the same mass but combined with the near-IR luminosity and a lower age of 40 Myr, they confirmed the evidence for a top-heavy IMF although with a looser requirement of  $m_{\text{low}} \approx 1 M_{\odot}$ . Similar investigations of young super star clusters in other systems, including NGC 1569A and NGC 1701-1 (Sternberg 1998), and five clusters in NGC 4038/4039 (Mengel et al. 2002), yielded mixed results as well. This seems to indicate a range of possible IMFs in super star clusters which may be related to their birth environment or to mass segregation (see, e.g., Mengel et al. 2002; McCrady et al. 2003). The results of the M 82 clusters may provide support in favour of an IMF flattening at low masses but, as pointed out by Smith & Gallagher (2001), it is unclear whether conclusions about luminous

star clusters, let alone of a handful only, can be extended to the overall pattern of star formation in the starburst.

Direct censuses of the low-mass star populations in Galactic and near-extragalactic high-mass star-forming regions are still scarce and difficult owing to the faintness of such stars and to important crowding effects. Recent results from very high sensitivity and angular resolution observations suggest that mere truncations of the IMF near  $1 M_{\odot}$  are not plausible, but the shape of the low-mass IMF remains poorly constrained. In particular, Brandl et al. (1999) found that the central parsec of NGC 3603 is well populated by pre-main sequence stars down to  $0.1 M_{\odot}$ , based on data from the Very Large Telescope. The near-IR adaptive optics observations by Eisenhauer et al. (1998) show no evidence for a significant flattening of the IMF down to their detection limit of  $1 M_{\odot}$ . In contrast, from deep *HST* images of the R 136 cluster in 30 Doradus, Sirianni et al. (1998, 2000) could probe the  $1.35 - 6.5 M_{\odot}$  range and reported a flattening of the IMF below  $2 M_{\odot}$ , a result however disputed by Selman et al. (1999). Given the shape of the solar-neighbourhood IMF, with possible turnover near  $0.5 M_{\odot}$  (e.g., Scalo 1986, 1998; Rana 1987; Kroupa 2001), and indications of a flattening towards lower masses in some local templates of starburst regions and super star clusters, our inferences for M 82 may not need be interpreted in terms of an “abnormal” deficiency of the IMF in low-mass stars.

## 5. SPATIALLY DETAILED MODELING OF M 82

The modeling of selected regions in the previous section provides the general characteristics of starburst activity in the central regions of M 82, but only an incomplete picture of its evolution. In particular, our choice of the small-scale regions as those with brightest continuum or line emission, and with deepest or shallowest CO bandheads likely introduced a bias towards preferential ages. In order to obtain a more complete picture, we modeled *individual regions throughout the entire 3D field of view*. These have a range in their properties suggesting a range in evolutionary states and burst strengths. Although along any line of sight the integrated properties will always

be dominated by the most luminous populations, a detailed modeling on small spatial scales reduces the bias towards particular ages.

Given our results of § 4, we assumed that a Salpeter IMF with high upper mass limits and burst decay timescales  $\lesssim 5$  Myr are appropriate for individual pixels. We also assumed that the near-IR properties are dominated everywhere by red supergiants. We emphasize again that the analysis of the  $M^*/L_K$  ratio of paper I strongly supports this hypothesis for the regions where the CO bandheads alone do not allow us to constrain the luminosity class of the evolved stars.

### 5.1. Spatial Distribution of the Burst Ages and Strengths

Figure 10 compares the data with single-burst models for  $m_{\text{up}} = 100 M_{\odot}$ , and  $t_{\text{sc}} = 1$  and 5 Myr, in the diagrams of neon,  $L_{\text{bol}}/L_{\text{Lyc}}$ , and  $L_K/L_{\text{Lyc}}$  ratios versus  $W_{2.29}$ . The size of the data points is proportional to the intrinsic  $L_K$ . We did not account for the contribution of the cool evolved stars to the bolometric luminosity of individual pixels, so that the values of  $L_{\text{bol}}^{\text{OB}}/L_{\text{Lyc}}$  are plotted in the  $L_{\text{bol}}/L_{\text{Lyc}}$  diagram.

A large fraction of the data points in all three diagrams do not fall on the model curves and exhibit the typical behaviour encountered for the selected regions: the neon and  $L_{\text{bol}}^{\text{OB}}/L_{\text{Lyc}}$  ratios imply significantly younger ages than  $W_{2.29}$ , with  $L_K/L_{\text{Lyc}}$  corresponding to intermediate ages. In the  $L_K/L_{\text{Lyc}}$  versus  $W_{2.29}$  diagram, the data points are distributed along a path that is remarkably parallel to the model curve for  $t_{\text{sc}} = 1$  Myr, but displaced towards lower  $L_K/L_{\text{Lyc}}$  by about an order of magnitude. Although the properties of some of the individual pixels could be reconciled with a single burst if the timescale is increased to values approaching 5 Myr, we have pursued with our hypothesis of sequential bursts. The data can be reproduced with two short successive bursts, with the young bursts producing about ten times more ionizing luminosity than the older bursts dominating the near-IR luminosity.

For each pixel, we therefore fitted a two-burst model to the constraints, each with  $t_{\text{sc}} = 1$  Myr, in the same manner as for the selected regions. We assigned an age of 1 Myr for  $L_{\text{bol}}^{\text{OB}}/L_{\text{Lyc}}$  ratios lower than the minimum  $L_{\text{bol}}/L_{\text{Lyc}}$  predicted by

the models (this is the case for a few pixels only). For the old bursts, we adopted the youngest solutions inferred from  $W_{2.29}$  and assigned the age of maximum  $W_{2.29}$  to the few pixels with EWs exceeding this limit. We estimated the formal uncertainties on the burst ages and initial star formation rates  $R_0$  by varying in turn the observational constraints in the ranges given by the measurements uncertainties.

Figure 11 presents the results. The ages for the young bursts range from 3.5 to 6.6 Myr, with an average of 4.8 Myr and dispersion of  $\sigma = 0.5$  Myr. The ages for the old bursts range from 7.2 to 12.6 Myr (the upper limit from the maximum  $W_{2.29}$ ), with an average of 8.8 Myr and dispersion of  $\sigma = 0.9$  Myr. Figure 12 shows the average burst age and total burst strength as a function of projected distance from the nucleus in a slit  $3''$ -wide along the galactic plane of M 82, as indicated in Figure 11. The typical uncertainties are  $\pm 0.5 - 1$  Myr for the ages and about 30% for the strengths. In view of these uncertainties, we conclude that the maps and profiles indicate roughly constant ages among the young bursts and among the old bursts, as well as nearly uniform strengths for the young bursts. Spatial variations in strength among the old bursts are more significant with, in particular, a clear peak around the nucleus consistent with our findings from the modeling of selected regions (§ 4.4).

Satyapal et al. (1997) investigated the spatial variations in ages from a dozen compact  $K$ -band emission sources, most of which are located within the regions mapped with 3D. They inferred burst ages in the range 4 – 10 Myr, with a trend of younger ages at larger projected radii. Given that they modeled the sources as single bursts and used the strength of the CO bandheads longwards of  $2.29 \mu\text{m}$  together with the EW of the Br $\gamma$  emission line at  $2.17 \mu\text{m}$  (inversely proportional to  $L_K/L_{\text{Lyc}}$ ), their results are consistent with ours.

### 5.2. The Global Star Formation History

From our spatially detailed modeling, we reconstructed the global star formation history within the 3D field of view by integrating the initial star formation rate  $R_0$  as a function of burst age  $t_b$  over all individual pixels. For sufficient sampling, we chose age bins increasing logarithmically by 0.05 dex. As long as the timescales assumed for all

individual bursts are similar and relatively short compared to the overall star formation history of interest, the integrated  $R_0(t_b)$  curve gives a measure of the “instantaneous” star formation rate at different times. Figure 13 shows the derived integrated starburst history together with the surface density of star formation rate, computed by dividing the integrated  $R_0(t_b)$  by the total area of the pixels contributing to each age bin. The results for the individual pixels are reproduced as well.

The integrated star formation rate exhibits two conspicuous peaks near 5 and 9 Myr, corresponding to distinct global starburst episodes. The first episode was globally 2.5 times stronger than the most recent one in terms of mass of stars formed. The star formation rate surface density reflects the nearly uniform strengths for the young bursts and the larger variations for the old bursts seen in Figures 11 and 12. We note that modeling the individual pixels with two short successive bursts introduces a bias towards separated burst events in the integrated star formation history. Again, such a scenario is however plausible in view of the spatial anticorrelation between the tracers of OB stars and those of cool evolved stars (§ 4.1).

The integrated star formation rate in the 3D field of view is well reproduced by two Gaussians in  $R_0$  versus age centered at 4.7 and 8.9 Myr, with amplitudes of 6.3 and 18.5  $M_\odot \text{ yr}^{-1}$  and full-widths at half-maximum of 1.1 and 1.7 Myr, respectively. These Gaussians are shown in Figure 13 along with the two-burst model fit to the integrated properties of the 3D field of view from § 4. The exponentially decaying functions provide reasonable though crude approximations to the detailed star formation history. In view of our results, it may not be surprising that Rieke et al. (1993) found that a double Gaussian profile optimized their model fits for the entire starburst core (with one of their best models reaching peak star formation activity near 5 and 13 Myr).

## 6. THE NATURE OF STARBURST ACTIVITY IN M 82

### 6.1. Star Formation Process

Observations of M 82 reveal important small-scale structure tracing individual burst sites on 10-pc or even parsec scales (see paper I). In particular, the ionized and molecular gas as well as

the IR-emitting dust exhibit clumpy morphologies on scales at least as small as 15 pc (e.g., Telesco & Gezari 1992; Larkin et al. 1994; Achtermann & Lacy 1995; Shen & Lo 1995). Compact continuum sources tracing clusters of red supergiants near their maximum luminosity are detected at near-IR wavelengths (e.g., Satyapal et al. 1997; McCrady et al. 2003). Optical imaging with *HST* has resolved over a hundred young super star clusters, some of which may lie in directions of lower extinction and belong to the inner starburst regions (O’Connell et al. 1995).

Our models show that the properties of individual burst sites are consistent with the formation of very massive stars and with short burst timescales of a few million years or less (see also Satyapal et al. 1997, for selected clusters). The typical sizes and the star formation parameters inferred make these burst sites comparable to Galactic and near-extragalactic massive star-forming regions such as NGC 3603 and the R 136 cluster in 30 Doradus.

Interestingly, the smoother and low-surface brightness emission regions make a substantial contribution to the integrated properties, suggesting that the prominent sub-structure may in fact trace the largest and most luminous burst sites. The diffuse ionized gas emission (notably in H recombination lines) and thermal dust emission represent about 50% of the respective total emission from the starburst core. The smoother and fainter stellar *K*-band continuum emission contributes at least as large a fraction to the total *K*-band luminosity. These components correlate roughly with the overall distribution of the brighter and more compact sources, and partly break up into smaller-scale structure at higher angular resolution (see, e.g., the *HST* NICMOS maps of Alonso-Herrero et al. 2003). Whether the diffuse emission in M 82, and more generally in starburst galaxies, traces large numbers of unresolved fainter compact sources or truly extended sources is still an open question, with implications for the importance of cluster formation in starbursts and subsequent dissolution in the stellar field (e.g., Ho & Fillipenko 1996; Meurer et al. 1995; Tremonti et al. 2001).

## 6.2. Evolution of Starburst Activity

### 6.2.1. Key Morphological Features

For a plausible evolutionary scenario of starburst activity in M82, our results must be interpreted together with the key morphological features:

- Large-scale tails and bridges of material emanating from M82 and connecting with its massive neighbour M81 located about 36 kpc in projection indicate gravitational interaction between the two galaxies (e.g., Yun, Ho, & Lo 1993, 1994).
- The morphology of the *K*-band emission, dominated by red supergiants, is highly suggestive of a nearly edge-on disk, peaks strongly towards the nucleus, and provides the strongest evidence for a  $\sim 1$  kpc-long stellar bar (e.g., Telesco et al. 1991; McLeod et al. 1993; Larkin et al. 1994). The brightest and most compact sources are mainly located in an “inner disk” within  $\approx 150$  pc of the nucleus and at the ends of the bar (e.g., Satyapal et al. 1997).
- The most prominent H II regions are concentrated in a rotating ring-like structure of radius  $\approx 85$  pc and, outside this ring, along ridges presumably on the leading edge of the rotating stellar bar (e.g., Larkin et al. 1994; Achtermann & Lacy 1995). The “ionized ring” is located just inside of the main concentrations of molecular gas in a toroid or tightly-wound spiral arms (e.g., Shen & Lo 1995). Our Br $\gamma$  source B2 coincides in projection with the western edge of the ionized ring while B1 is located farther out.
- The important population of young supernova remnants (SNRs) detected at radio wavelengths is quite uniformly distributed along the galactic plane over  $\approx 600$  pc (e.g., Kronberg, Biermann, & Schwab 1985; Muxlow et al. 1994). Their spatial distribution together with the ages derived for each starburst episode and the IMF weighting are more consistent with their being associated primarily with the populations of red supergiants throughout the disk.
- A bipolar outflow along the minor axis of M82 is traced out to at least 5 kpc by X-ray and optical observations (e.g., Bregman, Schulman, & Tomisaka 1995; Shopbell & Bland-Hawthorn 1998). The [Fe II]  $1.644\mu\text{m}$  emission exhibits a prominent arc-like structure to the south and centered near the nucleus. It may trace shock-ionized

iron-enriched gas where the outflowing wind interacts with interstellar disk material (e.g., Greenhouse et al. 1997; Alonso-Herrero et al. 2003).

- There is an apparent lack of gas and dust within the central few tens of parsecs of M82 (e.g., Telesco & Gezari 1992; Larkin et al. 1994; Shen & Lo 1995; Achtermann & Lacy 1995; Seaquist et al. 1996).

Given the relative distributions of the gaseous and stellar components and since M82 is viewed at an inclination angle of  $\approx 80^\circ$ , the two sequential bursts inferred locally and globally within the central starburst regions could be understood in terms of projection effects. In particular, the inner few tens of parsecs harbored the most intense starburst activity about 10 Myr ago and while more recent bursts appear superposed, they took place predominantly in circumnuclear regions at larger radii. The geometrical picture of M82 further emphasizes the particular intensity of the old nuclear burst revealed in Figures 11 and 12, with the red supergiants within the central few tens of parsecs in projection being physically close to the nucleus along the line of sight as well, while the OB stars — and the red supergiants elsewhere — possibly more extended along the line of sight. While alternatives could be advanced, we chose, in line with our two-burst hypothesis, to focus on the above interpretation as an illustrative yet possible case.

### 6.2.2. Triggering Mechanism

The primary triggering mechanism for starburst activity in M82 is generally attributed to the M82 – M81 tidal interaction  $\sim 10^8$  yr ago (e.g., Gottesman & Weliachew 1977; O’Connell & Mangano 1978; Lo et al. 1987; Yun et al. 1993, 1994). In this scenario, the ISM in M82 experienced strong large-scale torques and loss of angular momentum as it was transported towards the dynamical center of the galaxy, in accordance with numerical simulations (e.g., Sundelius et al. 1987; Noguchi 1987, 1988; Mihos & Hernquist 1996).

The increased cloud-cloud collision rate in the disk and the large amounts of material accumulated and compressed in the innermost regions could have led to the first starburst episode, characterized by very intense star formation at the nucleus and lower-level activity elsewhere in the disk. The nuclear burst and subsequent high rate of supernova explosions consumed rapidly the gas

supply and expelled the remaining gas via the starburst wind, thereby creating the central cavity in the ISM and preventing further star formation. The absence of a large concentration of radio SNRs in the nuclear vicinity is consistent with the lack of gas and dust.

### 6.2.3. *Subsequent Evolution*

Numerical simulations show that bars in galactic disks can be induced by galactic interactions and are very effective at driving material towards the central regions of galaxies (e.g., Combes & Gérin 1985; Noguchi 1987, 1988; Shlosman et al. 1989; Athanassoula 1992). Ring- or spiral-like dynamical resonances may develop under the action of such non-axisymmetric perturbations. In the presence of inner Lindblad resonances (ILRs), the radial inflow of material is stopped before it reaches the nucleus of the galaxy and accumulates in a circumnuclear ring. Star formation is triggered by shocks in the ring and along ridges leading the bar, and may be particularly enhanced at their intersections.

The second starburst episode in our models of M82 could thus be attributed to the presence of the bar and accompanying ILRs indicated by the global gas distributions (see also Lo et al. 1987; Telesco et al. 1991; Achtermann & Lacy 1995; Neininger et al. 1998). The ionized ridges presumably trace star formation sites on the leading side of the bar. Enhanced activity where the ISM streaming along the bar meets with the ionized ring may be hinted at by the slight increase in strength of the young bursts near B2 suggested by Figures 11 and 12 (see also Achtermann & Lacy 1995). The bar may have played a role during the first starburst episode by channeling the nuclear inflow before the present dynamical resonances appeared.

The apparent outward progression of starburst activity suggested by the sequence Nuclear supergiants  $\rightarrow$  Ionized ring  $\rightarrow$  Molecular ring may reflect the temporal development of the bar and redistribution of the mass as suggested by Telesco et al. (1991). At the radius of the ionized ring, the rotational velocity is about  $120 \text{ km s}^{-1}$  (Achtermann & Lacy 1995; Shen & Lo 1995). This implies an orbital period of  $4 - 5 \text{ Myr}$ , i.e. a dynamical timescale similar to the time elapsed between the peak star formation activity during the two recent

starburst episodes.

An alternative explanation could be self-induced propagation radially outward in the disk, as a consequence of the powerful nuclear burst and expanding shock wave generated by the massive stars winds and supernova explosions (e.g., Carlstrom & Kronberg 1991; Achtermann & Lacy 1995). Without dynamical resonances, the ISM may be expected to follow a smooth, radially decreasing density profile. Star formation triggered by an expanding “superbubble” in such a medium seems difficult to reconcile with pronounced and narrow peaks in the global star formation rate. The two peaks could perhaps reflect a sudden increase of mechanical energy release by the older nuclear burst after about  $5 \text{ Myr}$  but the contribution by massive star winds is already very substantial at ages  $< 5 \text{ Myr}$  before the first supernovae explode (e.g., Leitherer et al. 1999). Star formation activity along the ridges beyond the ionized ring is also difficult to explain in the self-induced outward propagation scenario.

We favoured bar-driven evolution as dominant mechanism because the stellar and gaseous components exhibit morphological features strongly supporting the existence of a bar and its dynamical effects. Bar-driven evolution has been proposed for other starburst systems as well as more quiescent spiral galaxies in which circumnuclear rings of enhanced gas density and star formation activity coexist with stellar or gaseous bars (e.g., Telesco & Decher 1988; Telesco, Dressel, & Wolsentcroft 1993; Knapen et al. 1995; Böker, Förster Schreiber, & Genzel 1997).

### 6.2.4. *Global Picture*

Investigations of regions outside of the central active starburst core outline further key elements for a global scenario. The integrated optical spectrum of M82 exhibits strong Balmer line transitions in absorption typical of A-type stars, indicative of an intermediate-age ( $0.1 - 1 \text{ Gyr}$ ) “post-starburst” population (Kennicutt 1992). de Grijs et al. (2000, 2001) used *HST* optical and near-IR data to study post-starburst regions  $0.5 - 1 \text{ kpc}$  northeast of the nucleus, identified as such from strong Balmer absorption lines and discontinuity in their spectra (O’Connell & Mangano 1978; Marcum & O’Connell 1996). The results of de Grijs and coworkers based on evolutionary synthesis



modeling of the photometric properties of compact luminous clusters and bright giant stars as well as their detection of candidate  $H\alpha$  SNRs imply that enhanced star formation occurred  $\sim 600$  Myr ago at radii of  $\sim 1$  kpc and up to  $\sim 30$  Myr ago near  $\sim 500$  pc. Gallagher & Smith (1999) modeled high-quality optical spectra of two super star clusters about 450 pc southwest of the nucleus and derived ages of  $\sim 60$  Myr.

In the framework of our models and interpretation, together with the spatial distribution of the radio SNRs and the  $M^*/L_K$  ratio, the first starburst episode  $\sim 10$  Myr ago was not strictly confined to the nuclear vicinity, but occurred throughout the central 500 pc as well. Along with the evidence from the post-starburst regions, this would support an “outside-inside-out” propagation of starburst activity in M82. The scenario we propose is summarized here and sketched in Figure 14.

- Following the gravitational interaction between M82 and M81,  $\sim 10^8$  yr ago, the ISM in M82 experienced strong large-scale torques, loss of angular momentum, and important infall towards the nuclear regions, leading to enhanced star formation activity in the central kiloparsec. The stellar bar induced by the interaction possibly played a role in channeling the inflow. In the absence of dynamical resonances, the infalling material can reach the nucleus.

- Within the central 500 pc of M82, a first starburst episode took place 8 – 15 Myr ago and was rapidly exhausted. The inner few tens of parsecs at the nucleus hosted the most intense star formation activity.

- A subsequent starburst episode was triggered predominantly by bar-induced dynamical resonances. It occurred 4 – 6 Myr ago, mainly in a circumnuclear ring and along the stellar bar, and also decayed rapidly.

- A supernova-driven starburst wind originating in the center of M82 has broken out of the galactic plane, the dramatic aftermath of the powerful nuclear burst. The outflow component in the disk may have played some role in triggering the second starburst episode.

### 6.3. Timescales and Feedback Effects

The global durations of  $\sim 10^6$  yr derived for each of the recent starburst episodes in M82 seem surprising for spatial scales up to at least 500 pc and in view of the longer estimates  $\sim 10^7 - 10^8$  yr often quoted for starburst systems (e.g., Thronson & Telesco 1986; Heckman 1998). We consider below three timescale arguments in trying to gain more insight into the quenching mechanisms of the recent starbursts in M82.

One argument relies on the comparison between the present star formation rate and the mass of the current gas reservoir, giving a “gas consumption timescale”  $\tau_{\text{gas}}$ . In M82, the gas is mostly in molecular form, with a total  $M_{\text{H}_2} = 1.8 \times 10^8 M_\odot$  (e.g., Wild et al. 1992). From our two-burst model of the starburst core (Table 4) and with a Salpeter IMF,  $M_{\text{stb}}^* \approx 2 \times 10^8 M_\odot$  of stars were formed in the past  $\approx 15$  Myr for  $m_{\text{low}} = 1 M_\odot$  and  $\approx 5 \times 10^8 M_\odot$  for  $m_{\text{low}} = 0.1 M_\odot$ . The latter value represents 80% of the measured stellar mass and, in view of the discussion of § 4.6, is here considered as an upper limit. The average star formation rate in the recent history of M82 is then  $R = 13 - 33 M_\odot \text{ yr}^{-1}$ , depending on  $m_{\text{low}}$ . Assuming 100% efficiency, starburst activity in M82 at the level observed in the past 15 Myr could be sustained for another  $\tau_{\text{gas}} \approx 5 - 15$  Myr. This provides a fair estimate for the minimum gas depletion timescale but has no connection with the physical processes responsible for the evolution of the starburst.

Considerations based on dynamical timescales are more closely linked to the large-scale mechanisms that may drive starburst activity. For a sample of 36 IR-selected starburst galaxies, Kennicutt (1998) inferred a median gas conversion efficiency of 30% per dynamical timescale, taken as an average orbital period for all objects of  $10^8$  yr;  $\epsilon_{\text{gas}} = 100\%/10^8$  yr occurs but in the most extreme objects. From the rotation curve of M82 (e.g., Götz et al. 1990; McKeith et al. 1993; Achtermann & Lacy 1995; Shen & Lo 1995; Neininger et al. 1998), we compute shorter dynamical timescales for regions inside the starburst core. For example, the orbital periods are about 5, 10, and 20 Myr at radii of 90, 225, and 500 pc corresponding to the locations of the ionized ring, of the main concentrations of molecular gas, and of

the outer limit enclosing the starburst core and most of the gas. The dynamics allow then for burst timescales of approximately  $\tau_{\text{dyn}} = 15$  Myr, 30 Myr, and 65 Myr for 30% efficiency per orbital period. Even with 100% efficiency, the timescales are barely short enough to explain the durations of each starburst episode in M82.

Such dynamical considerations may provide more insight concerning the settling time of the gas and the development of dynamical resonances. The orbital time at the radius of the ionized ring is similar to the time separation between the two most recent bursts. At radii 1 – 3 kpc, the orbital period is  $\approx 100 - 200$  Myr, which is of the order of the age of the super star clusters in the post-starburst regions  $\sim 1$  kpc northeast of the nucleus and to the epoch of last peri-passage between M82 and M81. The scenario proposed in § 6.2 for the triggering and propagation of the starburst episodes in M82 is consistent with these timescales.

None of the above arguments is however completely satisfactory for explaining the very short global burst durations suggested by our models. Most importantly, any feedback effect of massive stars via strong stellar winds and subsequent supernova explosions is neglected. Qualitatively, timescales of a few million years are similar to the lifetimes of stars with initial masses  $\gtrsim 50 M_{\odot}$ . Although both episodes took place over  $\sim 100 - 500$  pc scales, each was triggered nearly simultaneously everywhere, presumably as a result of brief gas compression events. Massive star winds and supernova explosions rapidly disrupting the remaining ISM locally, preventing further star formation after a few million years, may have “conspired” to produce a rapid decay of the global starburst activity as well.

We can make simple estimates for the “feedback timescale”  $\tau_{\text{feed}}$  by comparing the cumulative mechanical energy  $E_{\text{mech}}$  injected by supernovae (and neglecting the contribution by stellar winds) into the ISM with its gravitational binding energy  $E_{\text{bind}}$ , and assuming that starburst activity stops when they exactly balance each other:

$$\dot{E}_{\text{mech}} \tau_{\text{feed}} = E_{\text{bind}}, \quad (1)$$

where  $\dot{E}_{\text{mech}}$  is the rate of mechanical energy deposition. We assumed that all stars with initial masses  $\geq 8 M_{\odot}$  explode as supernovae with a

typical energy of  $10^{51}$  erg, of which a fraction  $\eta$  is transferred as kinetic energy to the ISM. For simplicity, we considered a spherically symmetric distribution of gas and stars within the starburst core, so that  $E_{\text{bind}} = (GM_{\text{dyn}}M_{\text{gas}})/\mathcal{R}$  where  $G$  is the gravitational constant,  $M_{\text{dyn}}$  and  $M_{\text{gas}}$  are the dynamical and gas masses, and  $\mathcal{R}$  is the radius of the region.

The rate of supernova explosions  $\nu_{\text{SN}}$  is the most direct tracer of  $\dot{E}_{\text{mech}}$  but the observed rates suffer from rather large uncertainties. We computed  $\dot{E}_{\text{mech}}$  using the inferred star formation rate  $R$  instead. The implicit assumption is that the burst is sufficiently evolved to have non-negligible  $\nu_{\text{SN}}$  and that the star formation rate is still substantial. For a Salpeter IMF between  $1 M_{\odot}$  and  $100 M_{\odot}$ ,  $\nu_{\text{SN}} [\text{yr}^{-1}] \approx 0.02 R [M_{\odot} \text{yr}^{-1}]$ . With these assumptions, Eq. 1 can be written:

$$\frac{\tau_{\text{feed}}}{\text{Myr}} \simeq 500 \left( \frac{f}{\eta} \right) \left( \frac{M_{\text{dyn}}}{10^{10} M_{\odot}} \right)^2 \left( \frac{\mathcal{R}}{\text{kpc}} \right)^{-1} \left( \frac{R}{M_{\odot} \text{yr}^{-1}} \right)^{-1}, \quad (2)$$

where  $f$  is the gas mass fraction. For the starburst core of M82,  $\mathcal{R} = 225$  pc,  $M_{\text{dyn}} \approx 8 \times 10^8 M_{\odot}$ , and  $M_{\text{gas}} \approx 1.8 \times 10^8 M_{\odot}$  (see paper I). With the average  $R \approx 13 M_{\odot} \text{yr}^{-1}$  derived for the appropriate IMF parameters, Eq. 2 yields  $\tau_{\text{feed}} \simeq 0.2\eta^{-1}$  Myr. The supernova efficiency is poorly constrained, but values in the range  $\eta = 0.1 - 1$  seem appropriate for M82 (Chevalier & Clegg 1985). Consequently,  $\tau_{\text{feed}} \simeq 0.2 - 2$  Myr. For comparison, with  $\nu_{\text{SN}} \approx 0.06 \text{ yr}^{-1}$  for M82, we obtain  $\tau_{\text{feed}} \simeq 1 - 10$  Myr depending on  $\eta$ . As alternative tracer, we can use  $L_{\text{bol}}$ . In a steady-state, our starburst models imply  $L_{\text{bol}} [L_{\odot}] \sim 10^{12} \nu_{\text{SN}} [\text{yr}^{-1}]$ , and thus  $R [M_{\odot} \text{yr}^{-1}] \sim 0.5 (L_{\text{bol}}/10^{10} L_{\odot})$ . With  $L_{\text{bol}} = 6.6 \times 10^{10} L_{\odot}$  for the starburst core, Eq. 2 implies  $\tau_{\text{feed}} \sim 1 - 10$  Myr as well. These estimates represent upper limits because we neglected massive stars winds.

The  $\tau_{\text{feed}}$  is more consistent than  $\tau_{\text{gas}}$  or  $\tau_{\text{dyn}}$  with the short durations in our models for the recent starburst episodes in M82. Admittedly, our  $\tau_{\text{feed}}$  estimates are also simplistic but they provide an additional perspective for the evolution of starburst activity and a possible explanation for short global burst durations. Along with our spatially detailed models, the above timescales are consistent with the overall progression of starburst activity in M82 being driven by large-scale dynamical

ical processes related to the tidal interaction with M 81 and the induced stellar bar, but suggests that once starburst activity was triggered, strong negative feedback effects acted very rapidly to inhibit further star formation on all spatial scales.

Recent studies of other starburst systems also provide evidence for short burst durations and for the episodic nature of starburst activity (e.g., Thornley et al. 2000; Böker et al. 1997; Vanzi et al. 1998; Alonso-Herrero et al. 2001). Some numerical simulations of the dynamical evolution of barred galaxies which account for the effects of star formation indicate a recurrent burst behaviour with typical timescale  $\sim 10^7$  yr, owing to the ability of massive stars to destroy the flow pattern when a sufficient number coexist in a given place (Heller & Shlosman 1994; Knapen et al. 1995).

## 7. SUMMARY

We have presented the results of detailed modeling of the central starburst regions of M 82, based on new near-IR integral field spectroscopy and mid-IR spectroscopy complemented with additional results taken from the literature. We applied starburst models optimized for observations in the range  $\lambda = 1 - 45 \mu\text{m}$  to these data and constrained the star formation parameters (cutoffs of the IMF, burst timescale) as well as the spatial and temporal evolution of starburst activity on scales as small as 25 pc.

Our data and models are consistent with the formation of very massive stars ( $\gtrsim 50 M_\odot$ ) and imply burst durations of at most a few million years for individual burst sites. With typical sizes on 10-pc scales or less, individual burst sites in M 82 are comparable to Galactic and near-extragalactic massive star-forming regions such as NGC 3603 and the R 136 cluster in 30 Doradus. For plausible limits on the mass involved in the starburst, we find that the IMF must flatten at low masses assuming a Salpeter slope at high masses. Dynamical information for three individual young stellar clusters in M 82 (Smith & Gallagher 2001; McCrady et al. 2003) provide similar evidence, but clearly more clusters need to be investigated. In view of the large uncertainties involved and the scarcity of low-mass IMF determinations in local high-mass star-forming regions, this result is difficult to interpret.

Among possible alternatives, our model results and interpretation together with the spatial distribution of the stellar and gaseous components in M 82 leads us to propose the following scenario. Globally, starburst activity in the central 500 pc of M 82 occurred during two successive episodes each lasting a few million years, about 10 and 5 Myr ago. The first episode took place throughout the disk and was particularly intense in the central few tens of parsecs. The second episode occurred predominantly in circumnuclear regions and along the stellar bar. We interpret this sequence in a tidally-triggered, bar-driven evolution scenario, consistent with the evidence for gravitational interaction between M 82 and its neighbour M 81, with the observed morphological signatures of the bar and associated dynamical resonances, and with the corresponding dynamical timescales.

The episodic nature of starburst activity and short global burst decay timescales in M 82 are particularly interesting results. Invoking a simple argument based on the comparison of the cumulative mechanical energy injected into the ISM and its gravitational binding energy, we find that the collective effect of massive stars winds and supernova explosions can disrupt the ISM in M 82 on timescales of  $\sim 10^6$  yr, providing a very efficient quenching mechanism for each starburst episode. Following brief gas compression events on large-scales, starburst activity decayed very rapidly due to its own strong negative feedback effects. Our scenario for M 82 outlines the interplay between the large-scale triggering mechanisms and the more local but important feedback effects in determining the evolution of starburst activity in this galaxy.

We would like to thank A. Pauldrach and R.-P. Kudritzki for providing us with their model atmospheres, G. Ferland for making CLOUDY version C90.05 available in advance of publication, and C. Telesco and D. Gezari for their  $12.4 \mu\text{m}$  data. It is a pleasure to thank M. Thornley, M. Lehnert, J. Gallimore, L. Tacconi, and L. Tacconi-Garman for stimulating discussions and useful comments, and to H. Spoon for help with using CLOUDY. We also wish to thank the referee, C. Leitherer, for a very considered and helpful report. This work was part of the Ph.D. thesis of NMFS, who acknowledges the Fonds pour les Chercheurs et l'Aide à

la Recherche (Gouvernement du Québec, Canada) for a Graduate Scholarship, and the Max-Planck-Institut für extraterrestrische Physik and Service d'Astrophysique of the CEA Saclay for additional financial support. SWS and the *ISO* Spectrometer Data Center at MPE are supported by DLR under grants 50 QI 8610 8 and 50 QI 9402 3. We also thank the German-Israeli Foundation for support of this work (grant I-551-186.07/97).

## A. FURTHER DETAILS ON STARS

### A.1. Spectral Energy Distributions

STARS computes the detailed SED intended for photoionization modeling of the nebular emission excited by the stars. The SEDs are taken from a hybrid grid generated as described by Thornley et al. (2000) from the LTE models of Kurucz (1992) for effective temperatures  $T_{\text{eff}} \leq 19,000$  K and the non-LTE models of Pauldrach et al. (1998) for  $T_{\text{eff}} \geq 25,000$  K, with SEDs for intermediate temperatures obtained by interpolation. The Pauldrach et al. models represent much better the effects of line blocking and blanketing in the rapidly expanding atmospheres of hot stars and are generally harder than the Kurucz models. A detailed description of the models and implications on the computed SEDs is given by Pauldrach et al. (2001) and references therein. The basic Pauldrach et al. model SEDs we used in STARS include dwarfs and supergiants. For dwarfs, they cover  $25000 - 60000$  K in  $T_{\text{eff}}$  at fixed surface gravity  $\log(g) = 4$  and mass-loss rates  $\dot{M}$  of  $10^{-8} - 5 \times 10^{-6} M_{\odot} \text{ yr}^{-1}$ . The ranges for supergiants are  $T_{\text{eff}} = 25000 - 50000$  K,  $\log(g) = 2.75 - 3.8$ , and  $\dot{M}$  of  $2 \times 10^{-6} - 1.5 \times 10^{-5} M_{\odot} \text{ yr}^{-1}$ . For a given  $T_{\text{eff}}$  and  $L_{\text{bol}}$  along a stellar track, STARS uses the corresponding evolutionary  $\log(g)$  and assigns the SED model with closest  $T_{\text{eff}}$  and  $\log(g)$  from the interpolated hybrid grid. The SED model grid covers well the range in parameters of the Geneva stellar tracks during most of the hot stars lifetimes (for both normal and enhanced mass-loss rates sets).

Various quantities predicted by STARS are derived using the empirical bolometric corrections of Schmidt-Kaler (1982) and the broad-band colours of Koornneef (1983). This is especially important for cool stars which have SEDs severely distorted by extensive molecular absorption and contaminated by thermal emission from a circumstellar dust shell that are not reproduced satisfactorily by black-body approximations or currently available model atmospheres. The impact of using empirical data is largest at near-IR wavelengths. For instance, the predicted  $K$ -band luminosities are up to 30% larger for the age range  $\sim 10 - 100$  Myr (assuming  $t_{\text{sc}} = 1$  Myr).

### A.2. Near-IR Stellar Absorption Features

STARS predicts the EWs of near-IR stellar absorption features characteristic of late-type stars: the  $^{12}\text{CO}$  (6,3) and  $^{12}\text{CO}$  (2,0) bandheads at  $1.62$  and  $2.29 \mu\text{m}$ , and the Si I, Na I, and Ca I features at  $1.59$ ,  $2.21$ , and  $2.26 \mu\text{m}$ . We implemented in STARS the EWs versus  $T_{\text{eff}}$  relationships for luminosity classes V, III, and I below  $5700$  K obtained by polynomial fitting to the homogeneized stellar data compiled by Förster Schreiber (2000). The EWs assigned to hotter stars were identically zero since the corresponding features vanish at higher  $T_{\text{eff}}$ . The exception is the  $1.59 \mu\text{m}$  feature but above  $\approx 6000$  K, the hydrogen Br14 transition is responsible for the absorption feature which has then a different physical meaning. The predicted EWs include “dilution” effects due to featureless continuum emission from OB stars and from associated free-free and free-bound processes. The stellar data are given for spectral resolutions of  $R \sim 1600$  and  $2500$  in the  $H$  and  $K$  band, respectively. For comparison with the models, EWs measured from lower resolution data should be corrected according to the relationships given by Förster Schreiber (2000).

Recently, Origlia et al. (1999) and Origlia & Oliva (2000) questioned the reliability of synthesis modeling of the CO bandheads from a critical analysis of theoretical modeling and observational data. They emphasized the importance of accounting for AGB evolution up to the end of the thermally-pulsing phase. They also demonstrated that uncertainties in stellar evolutionary tracks for red supergiant and AGB phases remain large especially at sub-solar metallicities but affect much less the results for ages up to  $\sim 10^7$  yr at near-solar metallicities. Since STARS accounts for the thermally-pulsing AGB (see below) and with the solar-metallicity tracks adopted in this work, these uncertainties are minimized in our predictions of the CO EWs.

### A.3. Implementation of the TP-AGB Phase

The Geneva tracks (Schaller et al. 1992) employed in STARS follow the evolution of stars up to well defined evolutionary phases. Tracks for massive stars ( $M > 7 M_{\odot}$ ) extend up to the end of the core carbon-burning phase, just prior to their explosion as core-collapse supernovae. Tracks for low-mass stars ( $M < 2 M_{\odot}$ ) end

at the helium flash which occurs at ages  $\gtrsim 10^9$  yr. The subsequent evolution of low-mass stars is not relevant for the starburst ages ( $< 10^9$  yr) we consider. For intermediate-mass stars ( $2 M_{\odot} < M < 7 M_{\odot}$ ), the Geneva tracks are terminated at the end of the early asymptotic giant branch (E-AGB), at ages in the range  $5 \times 10^7$  to  $10^9$  yr, and thus exclude the TP-AGB phase. TP-AGB stars can contribute significantly to the near-IR and total luminosities in starbursts, and so should be included in synthesis models (e.g., Charlot & Bruzual 1991; Maraston 1998; Origlia & Oliva 2000; Mouhcine & Lançon 2002). Observationally, there is growing evidence that such intermediate-age populations account for a non-negligible fraction of the integrated light in the central regions or bulges of several nearby galaxies, including our own (e.g., Freedman 1992; Blum, Sellgren, & DePoy 1996; McLean & Liu 1996; Lee 1996; Davidge et al. 1997; Martínez-Delgado & Aparicio 1998).

We extended the Geneva tracks for intermediate-mass stars using an approach suggested by Charlot & Bruzual (1991) which employs the analysis of the TP-AGB presented by Bedijn (1988). In this procedure, the TP-AGB is divided into a beginning “Mira phase” where the stars pulsate in the first overtone (or higher pulsation modes) while losing mass slowly, and a late “OH/IR” phase where the stars pulsate in the fundamental mode and lose mass rapidly. In the Mira phase, the stars increase in luminosity (and cool) and move up the AGB track appropriate for their mass. In the OH/IR phase, the luminosities do not vary much because of the rapid mass loss. Bedijn (1988) provides analysis and computations of the durations of each phase, including the maximum luminosities  $L_{\max}$  at the end of the OH/IR phase, as functions of the main-sequence masses between 2 and  $7 M_{\odot}$ . Using this information, we added two evolutionary points in the  $L_{\text{bol}}$  versus  $T_{\text{eff}}$  Hertzsprung-Russell diagram. The first point corresponds to the end of the Mira phase where (following Bedijn) we assume that  $L_{\text{bol}} = 0.8 L_{\max}$ . The second point corresponds to the end of the OH/IR phase where  $L_{\text{bol}} = L_{\max}$ . We obtained the effective temperature at each point from the  $L_{\text{bol}} - T_{\text{eff}}$  relations for stars on the AGB. Our extensions are illustrated in Figure 15. As sanity check, we compared the  $L_{\text{bol}}$  predicted by our shortest burst models based on conventional synthesis and by applying the fuel consumption theorem (Renzini & Buzzoni 1986) to our library of tracks. We obtain similar values within 10% on average up to  $10^9$  yr, with maximum differences of  $\pm 25\%$  at  $\leq 3 \times 10^8$  yr increasing to  $\pm 40\%$  at older ages where the numerical fluctuations due to the finite number of tracks become more important.

In attributing near-IR properties to TP-AGB stars, we followed a simple approach which can be justified by the small dispersion in  $T_{\text{eff}}$  of TP-AGB stars of various masses and the fact that the time spent in the OH/IR phase is at most 30% of the total TP-AGB lifetime according to Bedijn’s models (see also Charlot & Bruzual 1991). We assigned to all TP-AGB stars the average bolometric correction and broad-band colours of the prototypical Mira variable  $\omega$  Cet, derived from the data of Mendoza & Johnson (1965) and Zhou et al. (1984). For the EWs of near-IR absorption features, we adopted preliminary data obtained with the 3D instrument for a sample of Miras and other TP-AGB stars (S- and N-type stars). The observed CO bandhead strengths are comparable to those of the latest normal M-type giants. Similar conclusions are reached by inspection of the spectra published, e.g., by Lançon et al. (1999) and Lançon & Wood (2000). We therefore attributed the EWs of normal giants with  $T_{\text{eff}} = 3000$  K to all TP-AGB stars.

As expected, the effects of including the TP-AGB phase are most important for  $L_{\text{bol}}$  and for the near-IR properties while they are negligible for optical and UV properties. Figure 16 shows the TP-AGB contribution in our synthesized  $L_{\text{bol}}$ ,  $L_K$ , and  $W_{2.29}$ . Detailed comparison with other models including the TP-AGB, notably by Charlot & Bruzual (1991), Maraston (1998), and Mouhcine & Lançon (2002), is difficult because of the differences in synthesis techniques (conventional, isochrone, fuel consumption theorem) and in assumptions for TP-AGB stars (e.g.,  $T_{\text{eff}}$  scale, bolometric corrections, detailed evolution, lifetimes) among the various works. The time evolution and difference between  $L_{\text{bol}}$  and  $L_K$  of the TP-AGB contribution in our models agree qualitatively with these other models but the comparison suggests that the peak at  $\approx 5 \times 10^8$  yr for  $t_{\text{sc}} = 1$  Myr may be too narrow and with too large an amplitude. Around  $10^8$  yr, our short burst predictions lie in the ranges computed for coeval populations by the above authors, from a few to  $\sim 15\%$  for  $L_{\text{bol}}$  and  $\lesssim 10\%$  to  $\sim 40\%$  for  $L_K$  (with fairly large differences between different work). We point out that we implemented the TP-AGB to assess to first order the effects on the properties synthesized by STARS, and that our results of M82 would be essentially unchanged without it. Accurate modeling

would require a more careful and detailed treatment as presented by, e.g., Maraston (1998) and Mouhcine & Lançon (2002), as well as a better understanding of the properties and evolution of TP-AGB stars.

## REFERENCES

- Achtermann, J. M. & Lacy, J. H. 1995, *ApJ*, 439, 163
- Adelberger, K. L., & Steidel, C. C. 2000, *ApJ*, 544, 218
- Alonso-Herrero, A., Engelbracht, C. W., Rieke, M. J., Rieke, G. H., & Quillen, A. C. 2001, *ApJ*, 546, 952
- Alonso-Herrero, A., Rieke, G. H., Rieke, M. J., & Kelly, D. M. 2003, *AJ*, 125, 1210
- Athanassoula, E. 1992, *MNRAS*, 259, 345
- Augarde, R. & Lequeux, J. 1985, *A&A*, 147, 273
- Bedijn, P. J. 1988, *A&A*, 205, 105
- Bernlöhr, K. 1992, *A&A*, 263, 54
- Blum, R. D., Sellgren, K., & DePoy, D. L. 1996, *AJ*, 112, 1988
- Böker, T., Förster Schreiber, N. M., & Genzel, R. 1997, *AJ*, 114, 1883
- Brandl, B., et al. 1996, *ApJ*, 466, 254
- Brandl, B., Brandner, W., Eisenhauer, F., Moffat, A. F. J., Palla, F., & Zinnecker, H. 1999, *A&A*, 352, L69
- Bregman, J. N., Schulman, E., & Tomisaka, K. 1995, *ApJ*, 439, 155
- Bruzual A., G. & Charlot, S. 1993, *ApJ*, 405, 538
- Carlstrom, J. E. & Kronberg, P. P. 1991, *ApJ*, 366, 422
- Cerviño, M. & Mas-Hesse, J. M. 1994, *A&A*, 284, 749
- Chapman, S. C., Blain, A. W., Ivison, R. J., & Smail, I. R. 2003, *Nature*, 422, 695
- Charlot, S. & Bruzual A., G. 1991, *ApJ*, 367, 126
- Chevalier, R. A. & Clegg, A. W. 1985, *Nature*, 317, 44
- Colbert, J. W., et al. 1999, *ApJ*, 511, 721
- Combes, F. & Gérin, M. 1985, *A&A*, 150, 327
- Davidge, T. J., Rigaut, F., Doyon, R., & Cramp-ton, D. 1997, *AJ*, 113, 2094
- de Graauw, T., et al. 1996, *A&A*, 315, L49
- de Grijs, R., O’Connell, R. W., Becker, G. D., Chevalier, R. A., & Gallagher, J. S., III. 2000, *AJ*, 119, 681
- de Grijs, R., O’Connell, R. W., & Gallagher, J. S., III. 2001, *AJ*, 121, 768
- Devereux, N. A., Becklin, E. E., & Scoville, N. Z. 1987, *ApJ*, 312, 529
- Doane, J. S. & Mathews, W. G. 1993, *ApJ*, 419, 573
- Eisenhauer, F., Quirrenbach, A., Zinnecker, H., & Genzel, R. 1998, *ApJ*, 498, 278
- Engelbracht, C. W., Rieke, M. J., Rieke, G. H., Kelly, D. M., & Achtermann, J. M. 1998, *ApJ*, 505, 639
- Engelbracht, C. W., Rieke, M. J., Rieke, G. H., & Latter, W. B. 1996, *ApJ*, 467, 227
- Ferland, G. J. 1996, Hazy, a Brief Introduction to Cloudy, University of Kentucky Department of Physics and Astronomy Internal Report
- Fioc, M. & Rocca-Volmerange, B. 1997, *A&A*, 326, 950
- Förster Schreiber, N. M. 2000, *AJ*, 120, 2089
- Förster Schreiber, N. M., Genzel, R., Lutz, D., Kunze, D., & Sternberg, A. 2001, *ApJ*, 552, 544
- Freedman, W. L. 1992, *AJ*, 104, 1349
- Freedman, W. L. & Madore, B. F. 1988, *ApJ*, 332, L63
- Gaffney, N. I., Lester, D. F., & Telesco, C. M. 1993, *ApJ*, 407, L57
- Gallagher, J. S., III & Smith, L. J. 1999, *MNRAS*, 304, 540
- Gialalisco, M. 2002, *ARA&A*, 40, 579
- Giveon, U., Sternberg, A., Lutz, D., Feuchtgruber, H., & Pauldrach, A. W. A. 2002, *ApJ*, 566, 880



- Goldader, J. D., Joseph, R. D., Doyon, R., & Sanders, D. B. 1997, *ApJ*, 474, 104
- Götz, M., McKeith, C. D., Downes, D., & Greve, A. 1990, *A&A*, 240, 52
- Gottesman, S. T. & Weliachew, L. 1977, *ApJ*, 211, 47
- Greenhouse, M. A., et al. 1997, *ApJ*, 476, 105
- Grevesse, N. & Anders, E. 1989, in *AIP Conf. Proc. 183, Cosmic Abundances of Matter*, ed. C. J. Waddington (New York: AIP), 1
- Grevesse, N. & Noels, A. 1989, in *Origin and Evolution of the Elements*, ed. N. Prantzos, E. Vangioni-Flam, & M. Casse (Cambridge: Cambridge Univ. Press), 1
- Heckman, T. M. 1998, in *ASP Conf. Ser. 148, Origins*, ed. C. E. Woodward, J. M. Shull, & H. A. Thronson Jr. (San Francisco: ASP), 127
- Heckman, T. M., Armus, L., & Miley, G. K. 1990, *ApJS*, 74, 833
- Heller, C. H. & Shlosman, I. 1994, *ApJ*, 424, 84
- Hernquist, L. 1989, *Nature*, 340, 687
- Ho, L. C. & Filippenko, A. V. 1996, *ApJ*, 472, 600
- Hunt, L. K., Malkan, M. A., Moriondo, G., & Salvati, M. 1999, *ApJ*, 510, 637
- Hunter, D. A., Light, R. M., Holtzman, J. A., Lynds, R., O’Neil, E. J., Jr., & Grillmair, C. J. 1997, *ApJ*, 478, 124
- Kennicutt, R. C., Jr. 1992, *ApJ*, 388, 310
- Kennicutt, R. C., Jr. 1998, *ApJ*, 498, 541
- Kessler, M. F., et al. 1996, *A&A*, 315, L27
- Knapen, J. H., Beckman, J. E., Heller, C. H., Shlosman, I., & de Jong, R. S. 1995, *ApJ*, 454, 623
- Koornneef, J. 1983, *A&A*, 128, 84
- Kronberg, P. P., Biermann, P., & Schwab, F. R. 1985, *ApJ*, 291, 693
- Kroupa, P. 2001, *MNRAS*, 322, 231
- Kurucz, R. L. 1992, *Rev. Mex. Astron. Astrof.*, 23, 181
- Lançon, A., Mouhcine, M., Fioc, M., & Silva, D. 1999, *A&A*, 344, L21
- Lançon, A. & Rocca-Volmerange, B. 1994, *Ap&SS*, 217, 271
- Lançon, A., & Wood, P. R. 2000, *A&AS*, 146, 217
- Larkin, J. E., Graham, J. R., Matthews, K., Soifer, B. T., Beckwith, S., Herbst, T. M., & Quillen, A. C. 1994, *ApJ*, 420, 159
- Lee, M. G. 1996, *AJ*, 112, 1438
- Lehnert, M. D., Heckman, T. M., & Weaver, K. A. 1999, *ApJ*, 523, 575
- Leitherer, C., et al. 1999, *ApJS*, 123, 3
- Lo, K. Y., Cheung, K. W., Masson, C. R., Phillips, T. G., Scott, S. L., & Woody, D. P. 1987, *ApJ*, 312, 574
- Maraston, C. 1998, *MNRAS*, 300, 872
- Marcum, P., & O’Connell, R. W. 1996, in *ASP Conf. Ser. 98, From Stars to Galaxies: The Impact of Stellar Physics on Galaxy Evolution*, ed. C. Leitherer, U. Fritze-von Alvensleben, & J. Huchra (San Francisco: ASP), 419
- Martínez-Delgado, D. & Aparicio, A. 1998, *AJ*, 115, 1462
- Massey, P. & Hunter, D. A. 1998, *ApJ*, 493, 180
- McCraday, N., Gilbert, A. M., & Graham, J. R. 2003, *ApJ*, in press (astro-ph/0306373)
- McKeith, C. D., Castles, J., Greve, A., & Downes, D. 1993, *A&A*, 272, 98
- McLean, I. S. & Liu, T. 1996, *ApJ*, 456, 499
- McLeod, K. K., Rieke, G. H., Rieke, M. J., & Kelly, D. M. 1993, *ApJ*, 412, 111
- Mendoza, E. E., V., & Johnson, H. L. 1965, *ApJ*, 141, 161
- Mengel, S., Lehnert, M. D., Thatte, N., & Genzel, R. 2002, *A&A*, 383, 137

- Meurer, G. R., Heckman, T. M., Leitherer, C., Kinney, A., Robert, C., & Garnett, D. R. 1995, *AJ*, 110, 2665
- Meynet, G., Maeder, A., Schaller, G., Schaerer, D., & Charbonnel, C. 1994, *A&AS*, 103, 97
- Mihos, J. C. & Hernquist, L. 1994, *ApJ*, 431, L9
- Mihos, J. C. & Hernquist, L. 1996, *ApJ*, 464, 641
- Miller, G. E. & Scalo, J. M. 1979, *ApJS*, 41, 513
- Mouhcine, M., & Lançon, A. 2002, *A&A*, 393, 149
- Muxlow, T. W. B., Pedlar, A., Wilkinson, P. N., Axon, D. J., Sanders, E. M., & de Bruyn, A. G. 1994, *MNRAS*, 266, 455
- Nakagawa, T., Nagata, T., Geballe, T. R., Okuda, H., Shibai, H., & Matsuhara, H. 1989, *ApJ*, 340, 729
- Neininger, N., Guélin, M., Klein, U., García-Burillo, S., & Wielebinski, R. 1998, *A&A*, 339, 737
- Noguchi, M. 1987, *MNRAS*, 228, 635
- Noguchi, M. 1988, *A&A*, 203, 259
- O’Connell, R. W. & Mangano, J. J. 1978, *ApJ*, 221, 62
- O’Connell, R. W., Gallagher, J. S., III, Hunter, D., & Colley, W. N. 1995, *ApJ*, 446, L1
- Oliva, E., Origlia, L., Kotilainen, J. K., & Moorwood, A. F. M. 1995, *A&A*, 301, 55
- Olofsson, K. 1989, *A&AS*, 80, 317
- Origlia, L., Goldader, J. D., Leitherer, C., Schaerer, D., & Oliva, E. 1999, *ApJ*, 514, 96
- Origlia, L. & Oliva, E. 2000, *A&A*, 357, 61
- Papovich, C., Dickinson, M., & Ferguson, H. C. 2001, *ApJ*, 559, 620
- Pauldrach, A. W. A., Hoffmann, T. L., & Lennon, M. 2001, *A&A*, 375, 161
- Pauldrach, A. W. A., Lennon, M., Hoffmann, T. L., Sellmaier, F., Kudritzki, R.-P., & Puls, J. 1998, in *ASP Conf. Ser. 131, Properties of Hot Luminous Stars*, ed. I. Howarth (San Francisco: ASP), 258
- Prestwich, A. H., Joseph, R. D., & Wright, G. S. 1994, *ApJ*, 422, 73
- Puxley, P. J., Brand, P. W. J. L., Moore, T. J. T., Mountain, C. M., Nakai, N., & Yamashita, T. 1989, *ApJ*, 345, 163
- Puxley, P. J., Doyon, R., & Ward, M. J. 1997, *ApJ*, 476, 120
- Rana, N. C. 1987, *A&A*, 184, 104
- Renzini, A., & Buzzoni, A. 1986, in *Spectral Evolution of Galaxies*, ed. C. Chiosi & A. Renzini (Dordrecht: Reidel), 195
- Rieke, G. H., Lebofsky, M. J., Thompson, R. I., Low, F. J., & Tokunaga, A. T. 1980, *ApJ*, 238, 24
- Rieke, G. H., Loken, K., Rieke, M. J., & Tamblyn, P. 1993, *ApJ*, 412, 99
- Salpeter, E. E. 1955, *ApJ*, 121, 161
- Satyapal, S., Watson, D. M., Pipher, J. L., Forrest, W. J., Greenhouse, M. A., Smith, H. A., Fisher, J., & Woodward, C. E. 1997, *ApJ*, 483, 148
- Scalo, J. M. 1986, *Fund. Cosmic Phys.*, 11, 1
- Scalo, J. M. 1998, in *ASP Conf. Ser. 142, The Stellar Initial Mass Function*, ed. G. Gilmore & D. Howell (San Francisco: ASP), 201
- Schaller, G., Schaerer, D., Meynet, G., & Maeder, A. 1992, *A&AS*, 96, 269
- Schmidt-Kaler, T. 1982, *LB New Series, Vol. 2b, Astronomy and Astrophysics*, ed. K. Schaifers & H. H. Voigt (New York: Springer), 451
- Seaquist, E. R., Carlstrom, J. E., Bryant, P. M., & Bell, M. B. 1996, *ApJ*, 465, 691
- Sellmaier, F., Yamamoto, T., Pauldrach, A. W. A., & Rubin, R. H. 1996, *A&A*, 305, L37
- Selman, F., Melnick, J., Bosch, G., & Terlevich, R. 1999, *A&A*, 347, 532
- Shapley, A. E., Steidel, C. C., Adelberger, K. L., Dickinson, M., Giavalisco, M., & Pettini, M. 2001, *ApJ*, 562, 95
- Shapley, A. E., Steidel, C. C., Pettini, M., & Adelberger, K. L. 2003, *ApJ*, 588, 65

- Shen, J. & Lo, K. Y. 1995, *ApJ*, 445, L99
- Shlosman, I., Frank, J., & Begelman, M. C. 1989, *Nature*, 338, 45
- Shopbell, P. L. & Bland-Hawthorn, J. 1998, *ApJ*, 493, 129
- Sirianni, M., Nota, A., Leitherer, C., Clampin, M., & De Marchi, G. 1998, in *ASP Conf. Ser.* 131, *Properties of Hot Luminous Stars*, ed. I. Howarth (San Francisco: ASP), 363
- Sirianni, M., Nota, A., Leitherer, C., De Marchi, G., & Clampin, M. 2000, *ApJ*, 533, 203
- Smith, L. J., & Gallagher, J. S., III 2001, *MNRAS*, 326, 1027
- Sternberg, A. 1998, *ApJ*, 506, 721
- Sundelius, B., Thomasson, M., Valtonen, M. J., & Byrd, G. G. 1987, *A&A*, 174, 67
- Telesco, C. M., Campins, H., Joy, M., Dietz, K., & Decher, R. 1991, *ApJ*, 369, 135
- Telesco, C. M. & Decher, R. 1988, *ApJ*, 334, 573
- Telesco, C. M., Dressel, L. L., & Wolstencroft, R. D. 1993, *ApJ*, 414, 120
- Telesco, C. M. & Gezari, D. Y. 1992, *ApJ*, 395, 461
- Thornley, M. D., Förster Schreiber, N. M., Lutz, D., Genzel, R., Spoon, H. W. W., Kunze, D., & Sternberg, A. 2000, *ApJ*, 539, 641
- Thronson, H. A., Jr. & Telesco, C. M. 1986, *ApJ*, 311, 98
- Tremonti, C. A., Calzetti, D., Leitherer, C., & Heckman, T. M. 2001, *ApJ*, 555, 322
- Vanzi, L., Alonso-Herrero, A., & Rieke, G. H. 1998, *ApJ*, 504, 93
- Wamsteker, W. 1981, *A&A*, 97, 329
- Wei, A., Walter, F., Neininger, N., & Klein, U. 1999, *A&A*, 345, L23
- Weitzel, L., Krabbe, A., Kroker, H., Thatte, N., Tacconi-Garman, L. E., Cameron, M., & Genzel, R. 1996, *A&AS*, 119, 531
- Wild, W., Harris, A. I., Eckart, A., Genzel, R., Graf, U. U., Jackson, J. M., Russell, A. P. J., & Stutzki, J. 1992, *A&A*, 265, 447
- Wright, G. S., Joseph, R. D., Robertson, N. A., James, P. A., & Meikle, W. P. S. 1988, *MNRAS*, 233, 1
- Yun, M. S., Ho, P. T. P., & Lo, K. Y. 1993, *ApJ*, 411, L17
- Yun, M. S., Ho, P. T. P., & Lo, K. Y. 1994, *Nature*, 372, 530
- Zhou, K., Hao, Y., Chen, P., Zhang, Y., & Gao, M. 1984, *Ap&SS*, 107, 373

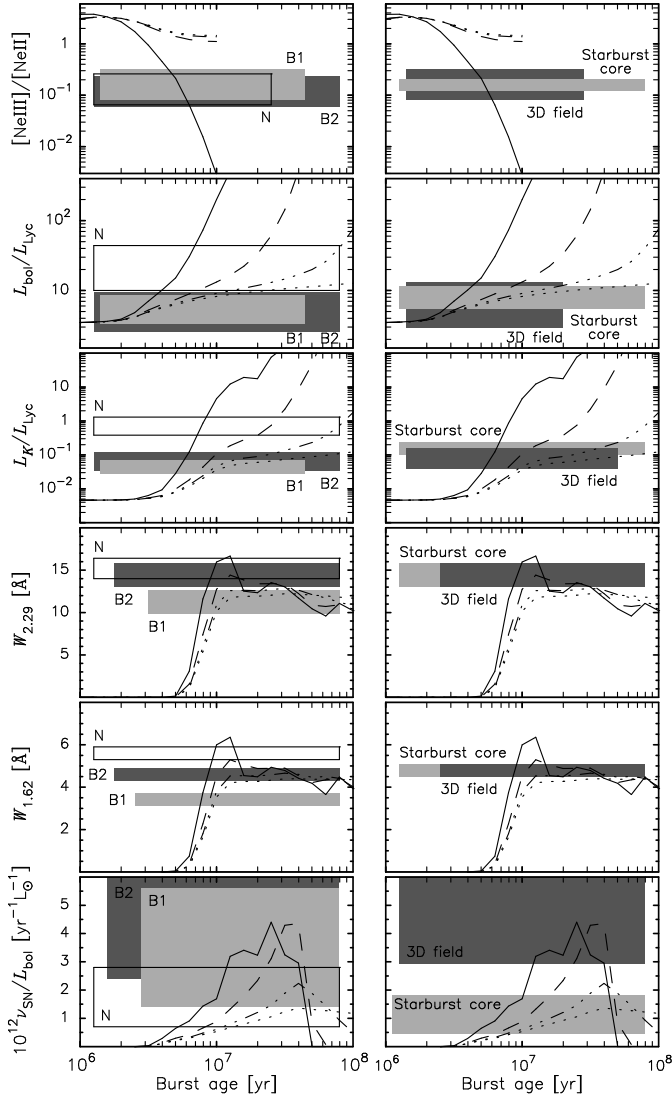


Fig. 1.— Comparison of the observed properties of selected regions in M82 with model predictions. The curves are computed for  $m_{\text{up}} = 100 M_{\odot}$  and four different burst decay timescales: 1 Myr (solid lines), 5 Myr (dashed lines), 20 Myr (dash-triple dot lines), and 1 Gyr (dotted lines). The other model parameters are given in Table 2. The horizontal bars indicate the measurements for the different regions as follows. In the left-hand side panels: central 35 pc at the nucleus (empty bars labeled “N”), B1 (light-shaded bars), and B2 (dark-shaded bars). In the right-hand side panels: the 3D field of view and the entire starburst core (dark- and light-shaded bars, respectively). The width of each bar corresponds to the formal uncertainties.

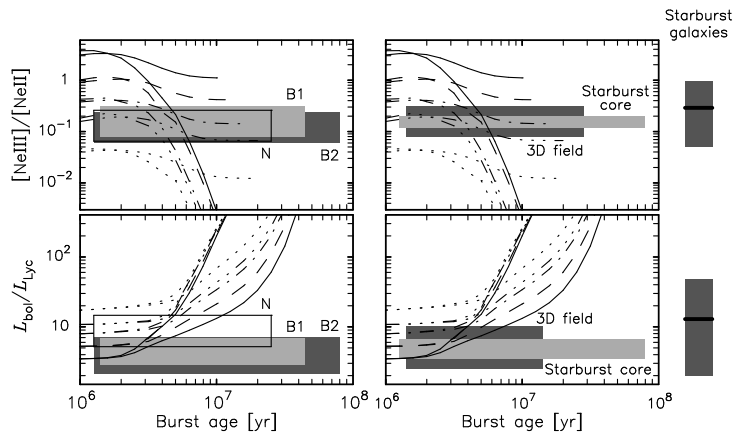


Fig. 2.— Comparison of the neon and  $L_{\text{bol}}^{\text{OB}}/L_{\text{Lyc}}$  ratios for selected regions in M82 with model predictions. The curves correspond to  $m_{\text{up}} = 100 M_{\odot}$  (solid lines),  $50 M_{\odot}$  (dashed lines),  $35 M_{\odot}$  (dash-dotted lines),  $30 M_{\odot}$  (dash-triple dot lines), and  $25 M_{\odot}$  (dotted lines); two burst timescales are illustrated: 1 and 5 Myr (steepest and shallowest curves, respectively). The horizontal bars within each plot indicate measurements for different regions as in Figure 1. The vertical bars and thick lines on the right-hand side of the figure show the ranges of and average ratios for the sample of solar-metallicity starburst galaxies observed with *ISO*-SWS by Thornley et al. (2000).

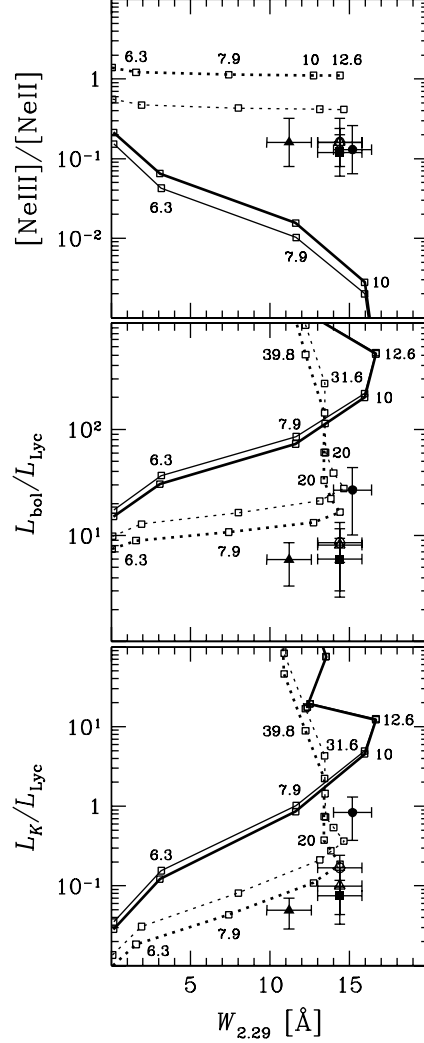


Fig. 3.— Single burst evolutionary tracks in diagrams of the neon,  $L_{\text{bol}}/L_{\text{Lyc}}$ , and  $L_K/L_{\text{Lyc}}$  ratios versus  $W_{2.29}$ . The data points with error bars indicate the measurements for the nucleus (filled circles), B1 (filled triangles), B2 (filled squares), the 3D field of view (open triangles), and the starburst core (open circles). The thick and thin curves correspond to models with  $m_{\text{up}} = 100$  and  $50 M_{\odot}$ , respectively. Two burst decay timescales are plotted for each  $m_{\text{up}}$ : 1 and 5 Myr (solid and dotted line pairs, respectively). The open squares along each curve indicate burst ages separated by logarithmic intervals of  $\Delta \log(t_b [\text{yr}]) = 0.1$  dex, with selected ages (in Myr) labeled for reference.

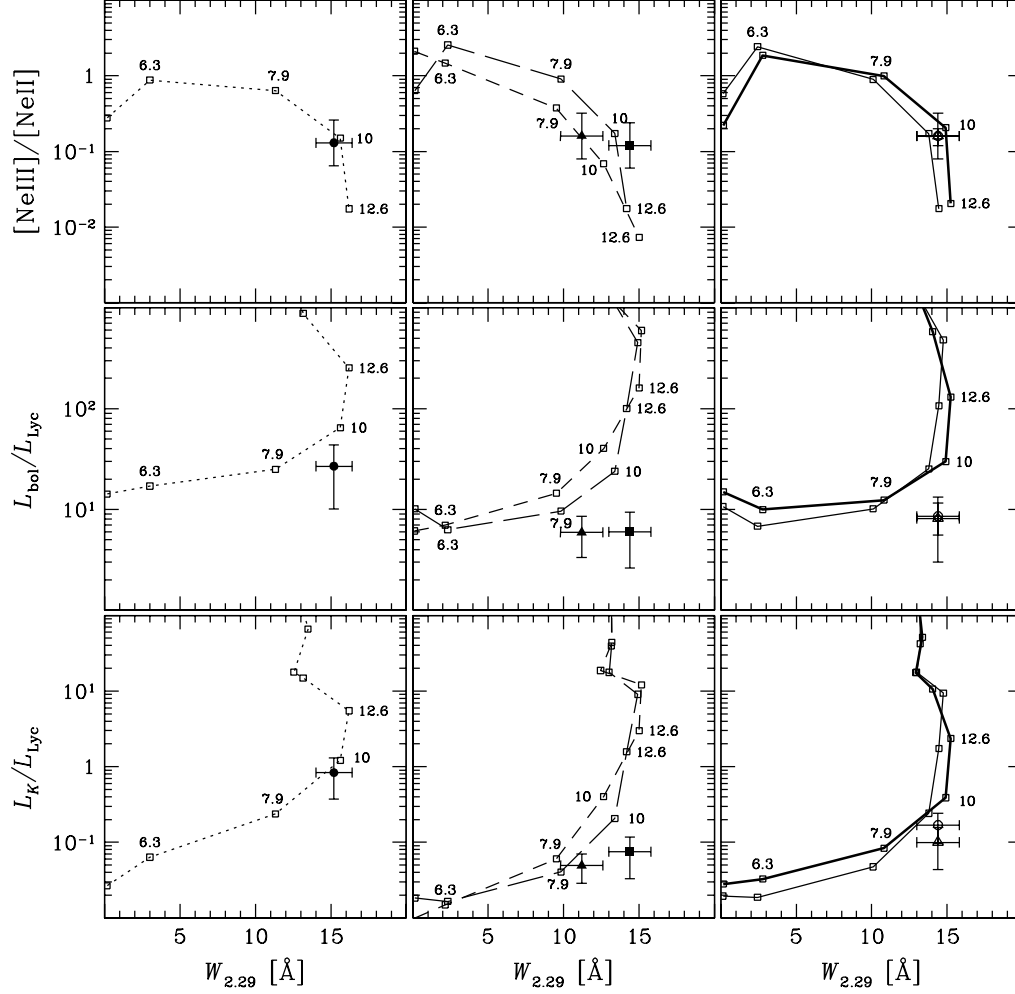


Fig. 4.— Two-burst model evolutionary tracks in diagrams of the neon,  $L_{\text{bol}}/L_{\text{Lyc}}$ , and  $L_K/L_{\text{Lyc}}$  ratios versus  $W_{2.29}$ . The data points with error bars indicate the measurements for the nucleus (left panels), B1 and B2 (center panels), and the 3D field of view and starburst core (right panels). The curves show the evolution of the properties for the combination of two bursts with best-fit time separation and relative intensities for each region (§ 4.4), each burst with  $t_{\text{sc}} = 1$  Myr and  $m_{\text{up}} = 100 M_{\odot}$ . Symbols and lines are as follows: filled circle and dotted line for the nucleus, filled triangle and short-dashed line for B1, filled square and long-dashed line for B2, open triangle and thin solid line for the 3D field of view, and open circle and thick solid line for the starburst core. The open squares and labels along each curve indicate the time in Myr since the onset of the older burst, in logarithmic intervals of  $\Delta \log(t_b [\text{yr}]) = 0.1$  dex.

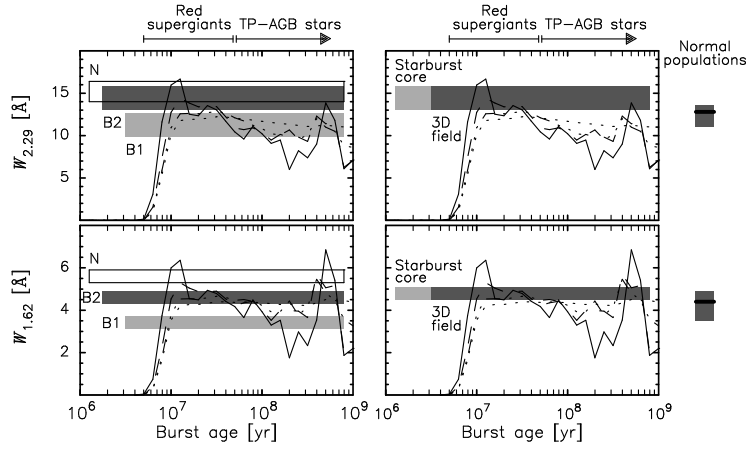


Fig. 5.— Comparison of the CO bandheads EWs of selected regions in M82 with model predictions. The data and model curves are the same as in Figure 1. A larger range of burst ages is shown to compare the EWs during the phases when red supergiants dominate the near-IR continuum and when intermediate-mass stars become important contributors, in particular TP-AGB stars. The vertical bars and thick lines on the right-hand side of the figure indicate the ranges of and average EWs observed for normal stellar populations characteristic of elliptical galaxies and bulges of spiral galaxies (Oliva et al. 1995). The sharp increase in synthesized EWs for  $t_{sc} \leq 20$  Myr around 500 Myr is most likely exaggerated due to the synthesis technique employed (see appendix A). Corresponding solutions are thus not considered valid and are also not supported by the mass-to- $K$ -band light ratio.



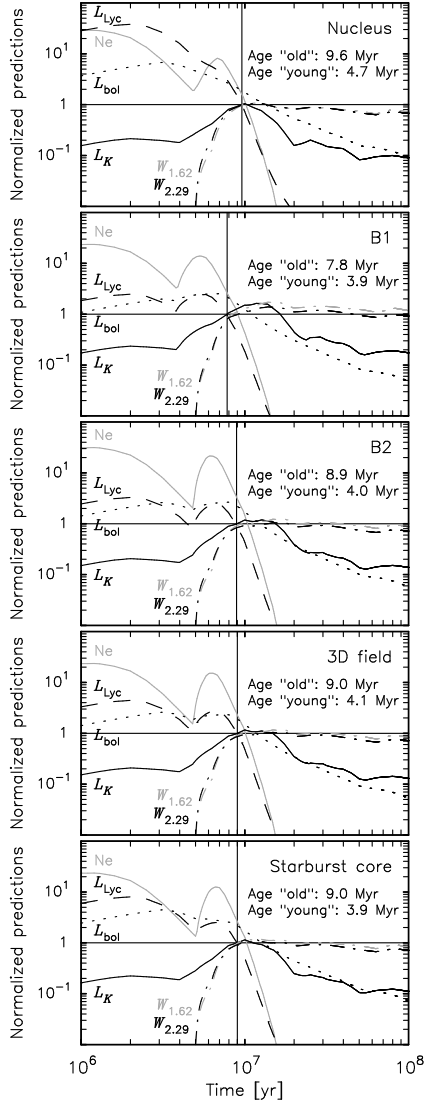


Fig. 6.— Starburst models for selected regions in M82. The curves in each plot represent the evolution of the properties for the two-burst model for each region (§ 4.4) as a function of the time elapsed since the onset of the oldest burst: neon ratio (grey solid lines labeled “Ne”),  $L_{\text{bol}}$  (black dotted lines),  $L_{\text{Lyc}}$  (black dashed lines),  $L_K$  (black solid lines), and  $W_{1.62}$  and  $W_{2.29}$  (grey and black dash-dotted lines, respectively). The ages for the bursts (“old” and “young”) are given in each diagram. The curves are normalized to the observed values; ideally, they should all meet at unity (horizontal line) at the appropriate age for the old burst (vertical line). An  $m_{\text{up}} = 100 M_{\odot}$  and  $t_{\text{sc}} = 1$  Myr were adopted for each burst.

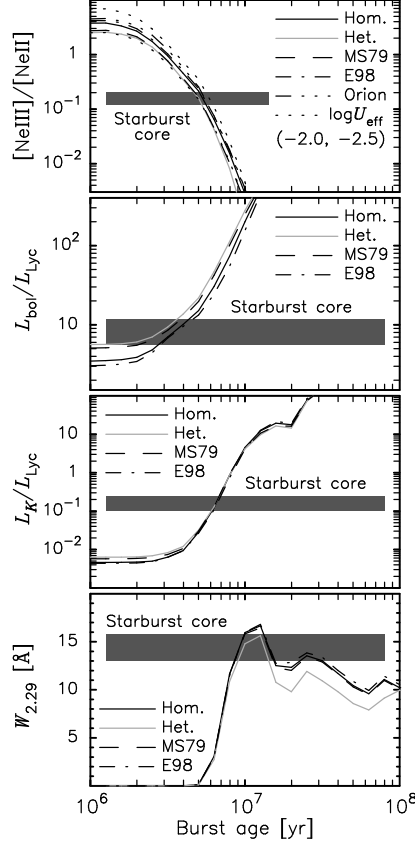


Fig. 7.— Effects of different model assumptions and parameters on the predictions of selected properties. For all models shown,  $m_{\text{up}} = 100 M_{\odot}$  and  $t_{\text{sc}} = 1 \text{ Myr}$ . The black solid curves represent the models applied to M82, computed assuming a homogeneous cluster population. The other curves show the effects of accounting for a heterogeneous cluster population following a plausible luminosity function (grey solid lines), and of adopting the IMF of Miller & Scalo (1979, dashed lines) or Eisenhauer et al. (1998, dash-dotted lines). Additional curves for the neon ratio were computed for a gas and dust composition typical of the Orion nebula (dashed-triple dot line) and for  $\log U_{\text{eff}} = -2$  dex and  $-2.5$  dex (upper and lower dotted lines, respectively). The properties of the starburst core of M82, representative of those of the other selected regions, are indicated by the horizontal bars.

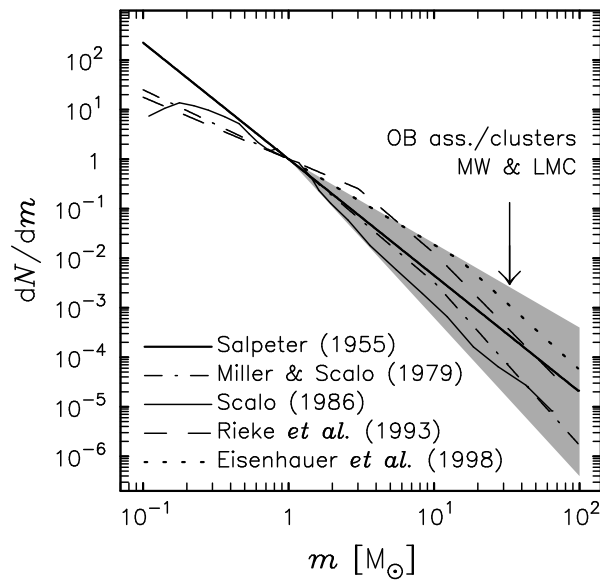


Fig. 8.— Comparison of various IMFs, represented by different lines as labeled in the plot. The IMFs are normalized to unity at  $1 M_{\odot}$ . The shaded area indicates the range of slopes determined in young clusters and OB associations in the Milky Way and in the Large Magellanic Cloud (Hunter et al. 1997 and references therein; Brandl et al. 1996; Eisenhauer et al. 1998; Massey & Hunter 1998; Scalo 1998).

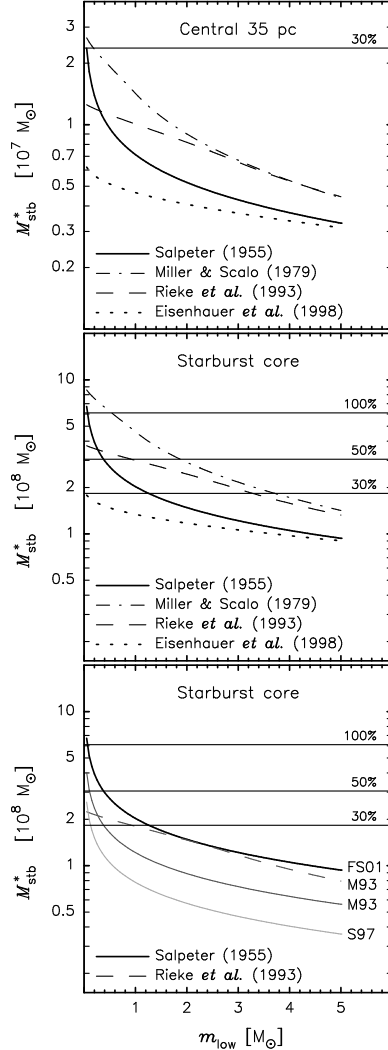


Fig. 9.— Predicted mass involved in the starburst as a function of  $m_{\text{low}}$ . The curves show the burst masses for the nucleus and the starburst core of M82 (central 35 and 500 pc) computed from the respective two-burst models normalized such that the predicted luminosities ( $L_K$  and  $L_{\text{Ly}\alpha}$ ) equal the observed luminosities for the derived burst ages (see Tables 3 and 4). Horizontal lines mark various fractions of the total stellar mass determined for each region ( $7.9 \times 10^7 M_\odot$  and  $6.1 \times 10^8 M_\odot$  for the central 35 pc and the starburst core, respectively). The top and middle panels show, for each region, the effects of adopting different IMFs, represented by the different curves as labeled in the plots. The bottom panel illustrates results obtained for the starburst core with a Salpeter (1955) IMF but assuming different values for the  $K$ -band luminosities (solid curves; “FS01”: this work, “M93”: McLeod et al. 1993, “S97”: Satyapal et al. 1997; see § 4.6); the dashed curve shows computations assuming the Rieke et al. (1993) IMF and McLeod et al. (1993)  $L_K$ .

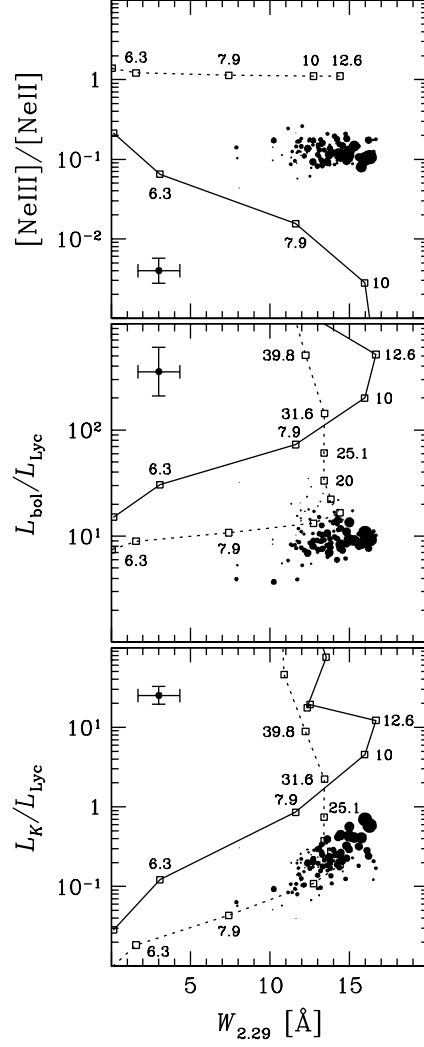


Fig. 10.— Properties of individual  $1'' \times 1''$  pixels within the 3D field of view. The diagrams are as in Figure 3, with model curves computed for a single burst with  $m_{\text{up}} = 100 M_{\odot}$ , and  $t_{\text{sc}} = 1$  and 5 Myr (solid and dashed lines, respectively); open squares indicate burst ages separated by  $\Delta \log(t_b [\text{yr}]) = 0.1$  dex, with selected ages (in Myr) labeled for reference. The size of the data points is proportional to the intrinsic stellar  $L_K$ . Typical uncertainties are shown by the error bars in each plot.

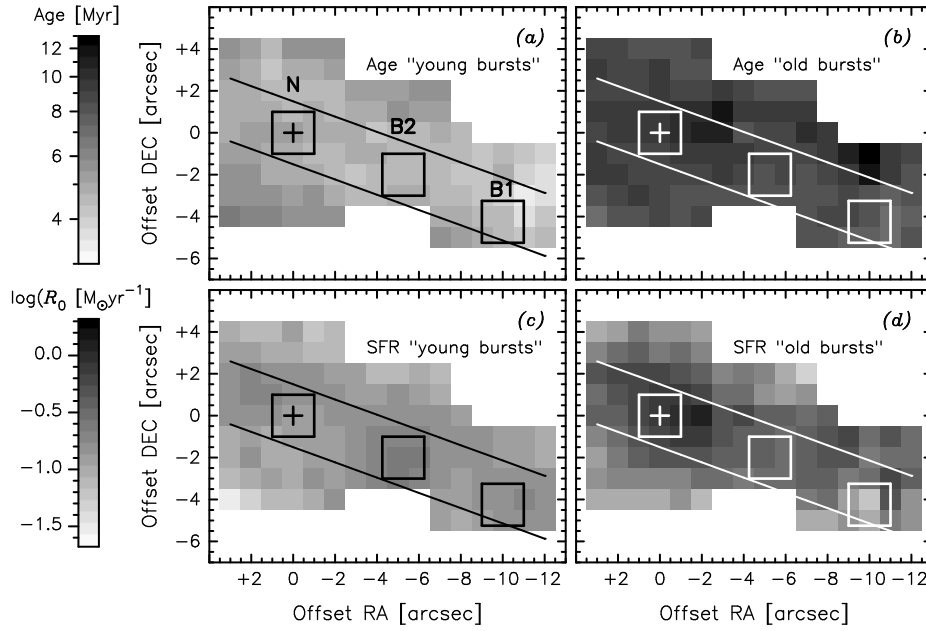


Fig. 11.— Model results for individual pixels in the 3D field of view. The top panels (*a* and *b*) show the derived ages for the young and old bursts while the bottom panels (*c* and *d*) show the initial star formation rates ( $R_0$ ). The cross marks the position of the nucleus and square boxes indicate selected regions modeled in § 4: the central 35 pc at the nucleus and regions B1 and B2. The diagonal lines indicate the  $3''$ -wide slit along the galactic plane of M82 used to extract the profiles shown in Figure 12.

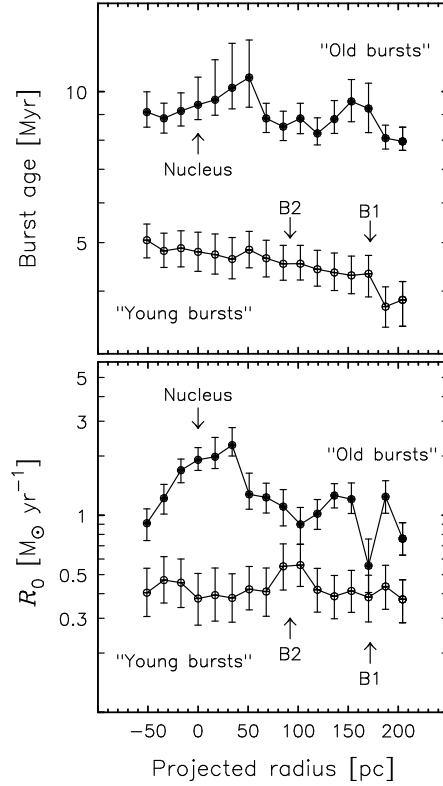


Fig. 12.— Variations of the burst age and strength with projected radius from the nucleus of M82. The radial profiles are obtained from the results of individual pixels in the  $3''$ -wide slit along the galactic plane shown in Figure 11. The results for the young and for the old bursts are represented by open and filled circles, respectively. The positions of the nucleus and of the regions B1 and B2 are indicated.

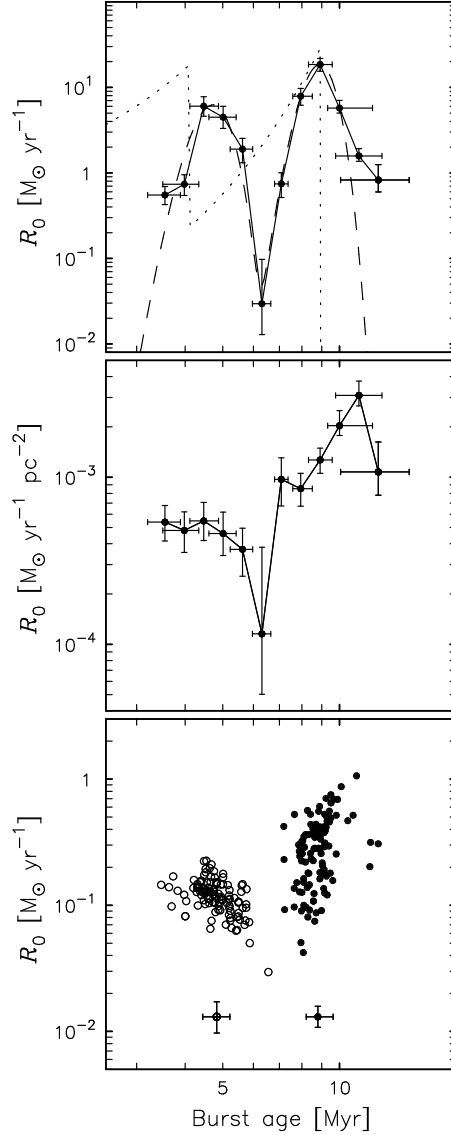


Fig. 13.— Global star formation history within the 3D field of view in M82. *Top panel*: integrated star formation rate derived from the spatially detailed modeling and double Gaussian profile which provides a good approximation thereof (solid line with filled dots and dashed line, respectively; see § 5.2). The best-fit two-burst model for the global properties of the 3D field of view is plotted for comparison (from Table 4; dotted line). *Middle panel*: initial star formation rate surface density, obtained by dividing the  $R_0$  versus burst age curve of the top panel by the total area of the pixels contributing in each age bin. *Bottom panel*: model results for the individual pixels, with open and filled circles representing the young and old bursts, respectively. Typical error bars are indicated at the bottom of the plot.



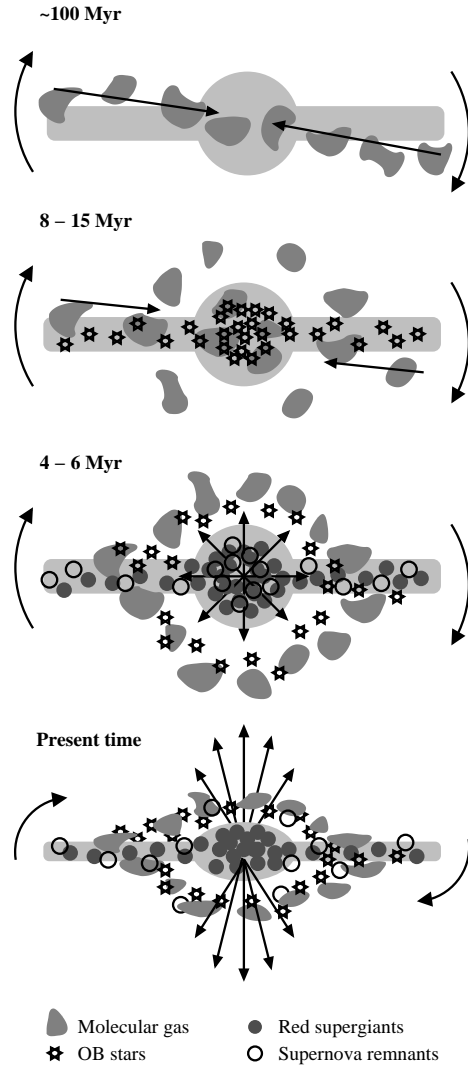


Fig. 14.— Sketch of the succession of events related to starburst activity in M82 depicted in § 6.2. The galaxy is illustrated as viewed from above the plane except for the bottom panel, where it is inclined to show the starburst wind.

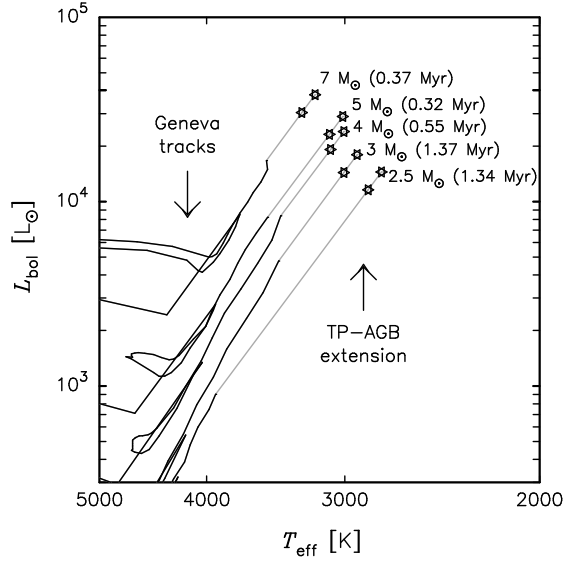


Fig. 15.— Selected evolutionary tracks in the theoretical Hertzsprung-Russell diagram for intermediate-mass stars. Black lines represent the Geneva tracks. Grey lines show our extensions to the TP-AGB phase computed from the prescriptions of Bedijn (1988); the star symbols correspond to the two evolutionary points associated with the different pulsation modes considered (appendix A). Total TP-AGB lifetimes are given in parenthesis.

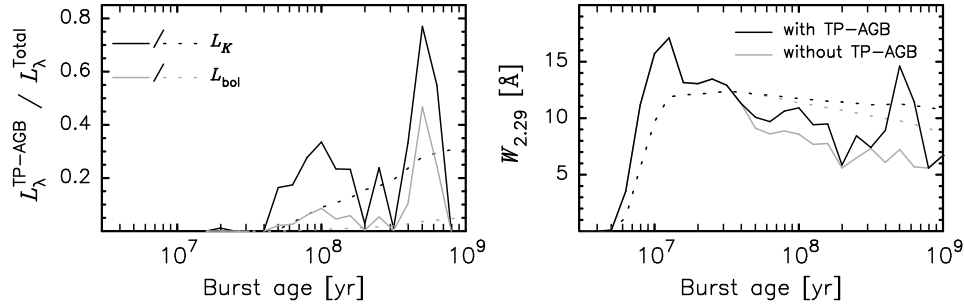


Fig. 16.— Effects of TP-AGB stars in our starburst models. The left panel shows the relative contribution of the TP-AGB phase to the total  $K$ -band and bolometric luminosities (black and grey lines, respectively). The right panel compares the model predictions for the EW of the CO bandhead at  $2.29 \mu\text{m}$  accounting for TP-AGB stars (black lines) and excluding TP-AGB stars (grey lines). Computations are shown for burst decay timescales of  $t_{\text{sc}} = 1$  Myr and 1 Gyr (solid and dotted lines, respectively). The effects of TP-AGB stars at ages  $\sim 500$  Myr for  $t_{\text{sc}} = 1$  Myr are likely exaggerated due to the conventional synthesis technique employed in our models (appendix A).

TABLE 1  
OBSERVATIONAL CONSTRAINTS FOR SELECTED REGIONS IN M 82

Property	Units	Nucleus	B1	B2	3D field	Starburst core
$L_K$	$10^8 L_\odot$	$0.56 \pm 0.23$	$0.074 \pm 0.024$	$0.15 \pm 0.05$	$2.7 \pm 0.8$	$13 \pm 4$
$L_{\text{Lyc}}$	$10^8 L_\odot$	$0.67 \pm 0.25$	$1.5 \pm 0.4$	$2.0 \pm 0.9$	$27 \pm 13$	$77 \pm 23$
$L_{\text{bol}}$	$10^8 L_\odot$	$18 \pm 9$	$8.9 \pm 3.1$	$12 \pm 4$	$220 \pm 90$	$660 \pm 120$
$L_{\text{bol}}^{\text{OB}}$	$10^8 L_\odot$	$6.6 \pm 2.0$	$7.4 \pm 2.2$	$9.2 \pm 2.7$	$170 \pm 60$	$390 \pm 40$
$M^*$	$10^8 M_\odot$	$0.79^{+0.22}_{-0.21}$	...	...	...	$6.1^{+2.7}_{-2.5}$
$\nu_{\text{SN}}^{\text{a}}$	$10^{-2} \text{yr}^{-1}$	0.25	0.25	0.58	13	6
$W_{1.62}$	$\text{\AA}$	$5.6 \pm 0.3$	$3.4 \pm 0.3$	$4.6 \pm 0.3$	$4.8 \pm 0.3$	$4.8 \pm 0.3$
$W_{2.29}$	$\text{\AA}$	$15.2 \pm 1.2$	$11.2 \pm 1.4$	$14.4 \pm 1.4$	$14.4 \pm 1.4$	$14.4 \pm 1.4$
$L_K/L_{\text{Lyc}}$	...	$0.84 \pm 0.46$	$0.049 \pm 0.021$	$0.075 \pm 0.042$	$0.10 \pm 0.06$	$0.17 \pm 0.07$
$L_{\text{bol}}/L_{\text{Lyc}}$	...	$27 \pm 17$	$5.9 \pm 2.6$	$6.0 \pm 3.4$	$8.1 \pm 5.1$	$8.6 \pm 3.0$
$L_{\text{bol}}^{\text{OB}}/L_{\text{Lyc}}$	...	$9.9 \pm 4.7$	$4.9 \pm 2.0$	$4.6 \pm 2.5$	$6.3 \pm 3.8$	$5.1 \pm 1.6$
$M^*/L_K$	$M_\odot/L_\odot$	$1.4 \pm 0.7$	...	...	...	$0.47 \pm 0.25$
$10^{12} \nu_{\text{SN}}/L_{\text{bol}}^{\text{a}}$	$\text{yr}^{-1}/L_\odot$	1.4	2.8	4.8	5.9	0.91
$[\text{Ne III}]/[\text{Ne II}]^{\text{b}}$	...	0.13	0.16	0.12	0.16	$0.16 \pm 0.04$

<sup>a</sup> Uncertainties of a factor of two are adopted for  $\nu_{\text{SN}}$  and  $10^{12} \nu_{\text{SN}}/L_{\text{bol}}$ .

<sup>b</sup> Values for the nucleus, B1, B2, and the 3D field of view are the inferred “equivalent ratios” as described in § 2. The uncertainties are estimated to be a factor of two.

TABLE 2  
SUMMARY OF MODEL PARAMETERS

Parameter	Symbol	Value
IMF: $dN/dm \propto m^{-\alpha}$		
Power-law index	$\alpha$	2.35 (Salpeter 1955)
Upper mass cutoff	$m_{\text{up}}$	$25 M_{\odot} - 100 M_{\odot}$
Lower mass cutoff	$m_{\text{low}}$	$0.1 M_{\odot} - 5 M_{\odot}$
Star formation history		
Burst timescale	$t_{\text{sc}}$	1 Myr – 1 Gyr
Burst age	$t_{\text{b}}$	1 Myr – 100 Myr
Burst strength <sup>a</sup>	$R_0$	...
Stellar properties		
Metallicity	...	Solar
Mass-loss rate	...	Normal
Nebular properties		
Electron density	$n_{\text{e}}$	$300 \text{ cm}^{-3}$
Ionization parameter <sup>b</sup>	$\log U_{\text{eff}}$	−2.3 dex
Inner radius <sup>b</sup>	$R_{\text{eff}}$	25 pc
Gas-phase abundances	...	Solar
Dust within nebulae	...	Neglected

<sup>a</sup> Characterized by the initial star formation rate.

<sup>b</sup> Effective values representing the local nebular conditions in the idealized thin gas shell geometry (see § 3.2).

TABLE 3  
STARBURST MODELS FOR THE NUCLEUS AND REGIONS B1 AND B2

Nucleus					
Parameter	Units	Young burst		Old burst	
$t_b$	Myr	$4.7 \pm 0.5$		$9.6^{+0.6}_{-0.2}$	
$R_0$	$M_\odot \text{ yr}^{-1}$	$0.52^{+0.30}_{-0.25}$		$6.6 \pm 1.5$	
Property	Units	Observed	Young burst	Old burst	Total
$L_K$	$10^8 L_\odot$	$0.56 \pm 0.23$	0.011	0.55	0.56
$L_{\text{Lyc}}$	$10^8 L_\odot$	$0.67 \pm 0.25$	0.48	0.16	0.64
$L_{\text{bol}}$	$10^8 L_\odot$	$18 \pm 9$	6.8	27	34
$M^*$	$10^8 M_\odot$	$0.79^{+0.22}_{-0.21}$	0.0052	0.066	0.071
$W_{1.62}$	$\text{\AA}$	$5.6 \pm 0.3$	0.0	5.6	5.5
$W_{2.29}$	$\text{\AA}$	$15.2 \pm 1.2$	0.0	15.2	14.9
$\nu_{\text{SN}}^a$	$10^{-2} \text{ yr}^{-1}$	0.25	0.038	0.45	0.49
$[\text{Ne III}]/[\text{Ne II}]^a$	...	0.13	0.25	0.0038	0.21
B1					
Parameter	Units	Young burst		Old burst	
$t_b$	Myr	$3.9^{+0.4}_{-0.6}$		$7.8^{+0.2}_{-0.1}$	
$R_0$	$M_\odot \text{ yr}^{-1}$	$0.84 \pm 0.26$		$0.96^{+0.27}_{-0.30}$	
Property	Units	Observed	Young burst	Old burst	Total
$L_K$	$10^8 L_\odot$	$0.074 \pm 0.024$	0.013	0.061	0.074
$L_{\text{Lyc}}$	$10^8 L_\odot$	$1.5 \pm 0.4$	1.4	0.083	1.5
$L_{\text{bol}}$	$10^8 L_\odot$	$8.9 \pm 3.1$	14	5.7	20
$M^*$	$10^8 M_\odot$	...	0.0082	0.0096	0.018
$W_{1.62}$	$\text{\AA}$	$3.4 \pm 0.3$	0.0	3.5	2.9
$W_{2.29}$	$\text{\AA}$	$11.2 \pm 1.4$	0.0	10.9	9.0
$\nu_{\text{SN}}^a$	$10^{-2} \text{ yr}^{-1}$	0.25	0.040	0.078	0.12
$[\text{Ne III}]/[\text{Ne II}]^a$	...	0.16	0.45	0.017	0.42
B2					
Parameter	Units	Young burst		Old burst	
$t_b$	Myr	$4.0^{+0.4}_{-0.5}$		$8.9 \pm 0.2$	
$R_0$	$M_\odot \text{ yr}^{-1}$	$1.2^{+0.5}_{-0.4}$		$1.7^{+0.4}_{-0.5}$	
Property	Units	Observed	Young burst	Old burst	Total
$L_K$	$10^8 L_\odot$	$0.15 \pm 0.05$	0.019	0.13	0.15
$L_{\text{Lyc}}$	$10^8 L_\odot$	$2.0 \pm 0.9$	1.8	0.067	1.9
$L_{\text{bol}}$	$10^8 L_\odot$	$12 \pm 4$	19	8.0	27
$M^*$	$10^8 M_\odot$	...	0.012	0.017	0.029
$W_{1.62}$	$\text{\AA}$	$4.6 \pm 0.3$	0.0	4.9	4.2
$W_{2.29}$	$\text{\AA}$	$14.4 \pm 1.4$	0.0	13.8	12.0
$\nu_{\text{SN}}^a$	$10^{-2} \text{ yr}^{-1}$	0.58	0.062	0.13	0.19
$[\text{Ne III}]/[\text{Ne II}]^a$	...	0.12	0.41	0.0067	0.40

<sup>a</sup> The adopted uncertainties for the constraints on the neon ratio and  $\nu_{\text{SN}}$  are a factor of two.

TABLE 4  
STARBURST MODELS FOR THE 3D FIELD OF VIEW AND THE STARBURST CORE

3D field of view					
Parameter	Units	Young burst		Old burst	
$t_b$	Myr	$4.1^{+0.5}_{-0.7}$		$9.0 \pm 0.2$	
$R_0$	$M_\odot \text{ yr}^{-1}$	$18^{+9}_{-8}$		$31^{+7}_{-8}$	
Property	Units	Observed	Young burst	Old burst	Total
$L_K$	$10^8 L_\odot$	$2.7 \pm 0.8$	0.30	2.4	2.7
$L_{\text{Lyc}}$	$10^8 L_\odot$	$27 \pm 13$	25	1.1	26
$L_{\text{bol}}$	$10^8 L_\odot$	$220 \pm 90$	280	140	420
$M^*$	$10^8 M_\odot$	...	0.18	0.31	0.49
$W_{1.62}$	$\text{\AA}$	$4.8 \pm 0.3$	0.0	5.0	4.4
$W_{2.29}$	$\text{\AA}$	$14.4 \pm 1.4$	0.0	14.0	12.4
$\nu_{\text{SN}}^a$	$10^{-2} \text{ yr}^{-1}$	13	0.99	2.3	3.3
$[\text{Ne III}]/[\text{Ne II}]^a$	...	0.16	0.38	0.0061	0.37
Starburst core					
Parameter	Units	Young burst		Old burst	
$t_b$	Myr	$3.9^{+0.2}_{-0.3}$		$9.0 \pm 0.2$	
$R_0$	$M_\odot \text{ yr}^{-1}$	$43 \pm 11$		$160 \pm 30$	
Property	Units	Observed	Young burst	Old burst	Total
$L_K$	$10^8 L_\odot$	$13 \pm 4$	0.66	12	13
$L_{\text{Lyc}}$	$10^8 L_\odot$	$77 \pm 23$	69	5.8	75
$L_{\text{bol}}$	$10^8 L_\odot$	$660 \pm 120$	710	740	1500
$M^*$	$10^8 M_\odot$	$6.1^{+2.7}_{-2.5}$	0.42	1.6	2.0
$W_{1.62}$	$\text{\AA}$	$4.8 \pm 0.3$	0.0	5.0	4.7
$W_{2.29}$	$\text{\AA}$	$14.4 \pm 1.4$	0.0	14.0	13.3
$\nu_{\text{SN}}^a$	$10^{-2} \text{ yr}^{-1}$	6	2.1	12	14
$[\text{Ne III}]/[\text{Ne II}]^a$	...	$0.16 \pm 0.04$	0.45	0.0061	0.42

<sup>a</sup> The adopted uncertainties for the constraints on the neon ratio for the 3D field of view and on  $\nu_{\text{SN}}$  for both regions are a factor of two.

TABLE 5  
PARAMETERS FOR VARIOUS IMFs<sup>a</sup>

Source	$\alpha_1$	$m_1$ ( $M_\odot$ )	$\alpha_2$	$m_2$ ( $M_\odot$ )	$\alpha_3$
Salpeter 1955	2.35	...	...	...	...
Miller & Scalo 1979	1.4	1	2.5	10	3.3
Rieke et al. 1993	1.25	3	2.5	10	3.0
Eisenhauer et al. 1998	1.73	15	2.7	...	...

<sup>a</sup> The IMFs are represented by a power-law  $dN/dm \propto m^{-\alpha}$ . The values of  $\alpha_i$  give the power-law indices for different mass ranges and the  $m_i$  correspond to the inflection points for broken power-laws.